

Article

# Self-Coagulation Theory and Related Comet- and Semi-Circle-Shaped Structures in Electronegative and Gaseous Discharging Plasmas in the Laboratory

Yu Tian<sup>1</sup> and Shuxia Zhao<sup>2,\*</sup> 

<sup>1</sup> Experimental Training Center, Dalian University of Science and Technology, Dalian 116052, China; tianyu@dlust.edu.cn

<sup>2</sup> School of Physics, Dalian University of Technology, Dalian 116024, China

\* Correspondence: zhaonie@dlut.edu.cn; Tel.: +86-15840698390

**Featured Application:** Silicon-based material etching and thin film deposition.

**Abstract:** In this work, the two-dimensional fluid models for two types of inductively coupled plasma, Ar/O<sub>2</sub> and Ar/SF<sub>6</sub>, are numerically solved by the finite element method. Four interesting phenomena revealed by the simulations are reported: (1) comet-shaped and semi-circle-shaped structures in Ar/O<sub>2</sub> and Ar/SF<sub>6</sub> plasmas, respectively; (2) blue sheaths that surround the two structures; (3) the collapse and dispersion of semi-circle-shaped structures of certain Ar/SF<sub>6</sub> plasma cations and anions when they are observed separately; and (4) the rebuilding of coagulated structures by minor cations in the Ar/SF<sub>6</sub> plasma at the discharge center. From the simulation detail, it was found that the cooperation of free diffusion and negative chemical sources creates the coagulated structure of anions, and the self-coagulation theory is therefore built. The advective and ambipolar types of self-coagulation are put forth to explain the co-existence of blue sheath and internal neutral plasma, among which the advective type of self-coagulation extends the Bohm's sheath theory of cations to anions, and the ambipolar type of self-coagulation originates from the idea of the ambipolar diffusion process, and it updates the recognition of people about the plasma collective interaction. During the ambipolar self-coagulation, each type of Ar/SF<sub>6</sub> plasma cations and anions is self-coagulated, and the coagulated plasma species are then modeled as mass-point type (or point-charge type, more precisely). When the charge amounts of two point-charge models of plasma species with the same charge type are equal, the expelling effect caused by the Coulomb's force of them leads to the collapse or dispersal of heavily coagulated species. The simulation shows that the lighter the species is, the easier it self-coagulates and the more difficult its coagulation is broken, which implies the inertial effect of density quantity. Moreover, the collapse of cation coagulation creates the spatially dispersed charge cloud that is not shielded into the Debye's length, which indicates the anti-collective behavior of electronegative plasmas when they are self-coagulated. The rebuilt coagulated structure of minor Ar/SF<sub>6</sub> plasma species at the discharge center and the weak coagulation of electrons in the periphery of the main coagulated structure that is under the coil are caused by the monopolar and spontaneous (non-advective) type of self-coagulation. The analysis predicts an intensity order of physically driven coagulation force, chemical self-coagulation force, and ambipolar self-coagulation force. The popular coagulated structure of the electronegative ICP sources is urgently needed to validate the experiment.



**Citation:** Tian, Y.; Zhao, S.

Self-Coagulation Theory and Related Comet- and Semi-Circle-Shaped Structures in Electronegative and Gaseous Discharging Plasmas in the Laboratory. *Appl. Sci.* **2024**, *14*, 8041. <https://doi.org/10.3390/app14178041>

Academic Editor: Gerard Ghibaudo

Received: 20 August 2024

Revised: 4 September 2024

Accepted: 5 September 2024

Published: 8 September 2024



**Copyright:** © 2024 by the authors. Licensee MDPI, Basel, Switzerland. This article is an open access article distributed under the terms and conditions of the Creative Commons Attribution (CC BY) license (<https://creativecommons.org/licenses/by/4.0/>).

**Keywords:** self-coagulation; comet- and semi-circle-shaped structures; advective ambipolar type; blue sheath; decouple of electrons dynamics; electrically expelling force; mass-point model; inertial effect of density quantity; anti-collective behavior; spontaneous monopolar type; electronegative plasmas; fluid simulation

## 1. Introduction

The low-pressure and electronegative radio frequency plasma sources are widely used in the Si-based material etching process and functional thin film deposition [1,2]. In general, the capacitive [3] and inductive radio frequency sources are applied, and the inductively coupled plasma [4,5] (abbreviated as ICP) is characterized by its low-pressure discharge, high plasma density, simple device, etc. Due to the interference of negative ions (anions), the transport process and discharge structure of electronegative and gaseous discharging plasma are quite different from the electropositive plasma. In Ref. [6], based on an ambipolar diffusion of triple species (electron, cation, and anion) in highly electronegative plasma, the parabola discharge theory was established by Lieberman and Lichtenberg. Later in Ref. [7], they built the ellipse theory again for the highly electronegative plasma in the case that the Boltzmann's balance is not reasonable for the anions. In Ref. [8], they still found internal sheaths existing in electronegative plasma, and the structure of the non-neutral region varied significantly with the ratios of anion and electron densities and of their temperatures. In addition, the phenomenon of stratification through the electronegative core and electropositive halo in the whole discharge region was recognized in Refs. [6–9]. Moreover, a double-layer structure was founded by Sheridan at the interface of the core and halo, and the electronegative plasma was then called double-layer-stratified discharge [10]. Of more interest is that the double layer was accompanied by the oscillation of the electropositive halo. Chabert (utilizing the kinetic model) and Franklin finally concluding the oscillation was an artifact, respectively [11,12]. In addition, the negative ion front model was established by Kaganovich at observing the temporal evolution of the electronegative plasma density border in Ref. [13]. The above discharge structure theories of electronegative plasma are based on quasi-direct current discharge, such as ICP sources. When the electronegative plasma oscillates, such as in the CCP source, the famous drift-ambipolar (abbreviated as DA) and striation discharging models were found by Schulze [14] and Liu [15], respectively.

Besides the above interesting mechanisms constructed in electronegative plasma, our recent works revealed the coagulated structure, such as the comet shape of anions, in the Ar/O<sub>2</sub> ICP source (with low electronegativity) by means of a fluid model [16,17]. In these references, the self-coagulation idea was for the first time suggested to explain the formation of coagulated structure in the plasma background that is dispersed. In the present article, the self-coagulation theory is formally put forward to interpret the related coagulated structures in general electronegative plasmas, such as the Ar/SF<sub>6</sub> plasma with high electronegativity. Our fluid simulation and theoretic analysis both reveal the significance of ratio of ionic recombination loss in the chemical source, which somehow determines the discharge structure. In particular, if it is neglected, the discharge structure is described by parabola theory. If it is comparative to the generation of cation (ionization), the discharge is described by ellipse theory. Furthermore, if this loss rate is larger than the generation rate, the self-coagulation behavior happens and the coagulated structure is then formed. More of interest is that the coagulated structure, such as a semi-circle in Ar/SF<sub>6</sub> plasma, perhaps collapses at the expelling interaction that is caused by the Coulomb's force. The phenomenon of plasma coagulation discovered herein helps correlate again the gaseous discharging plasma in the laboratory and astrophysics plasma in the universe, in addition to the double layer that is used to accelerate the cosmic particle, and meanwhile, it appears in the expanded ICP source [18,19] and shock (by means of multifluid model and transport theory) [20,21].

This article is outlined as follows: In Section 2, the used fluid model for the ICP source and chemical reactions for Ar/O<sub>2</sub> and Ar/SF<sub>6</sub> plasmas are given. In Section 3.1, the first simulated phenomenon is given, i.e., the comet-shaped structure found in the Ar/O<sub>2</sub> ICP source, which is characterized by the free diffusion and negative chemical source (recombination loss of anions). The dimensional analysis shows that the recombination can be transferred into drift flux and then balance the free diffusion. This forms a static and mechanical balance between the physics and chemistry. Furthermore, in the related discussion of Section 4.1, the self-coagulation theory is built via the free diffusion and

negative chemical source, which explains mathematically the formations of both the comet- and semi-circle-shaped coagulated structures (see Section 3.2).

In Section 3.2, the second simulated phenomenon is given, i.e., the blue sheaths found in Ar/O<sub>2</sub> and Ar/SF<sub>6</sub> ICP sources. In the Ar/O<sub>2</sub> plasma, the coagulated structure is comet-shaped, and a blue sheath surrounds it. In the Ar/SF<sub>6</sub> plasma, the coagulated structure is semi-circle-shaped, and the blue sheath still surrounds it. In both cases, the plasmas surrounded by the blue sheaths are both electrically neutral. For explaining the blue sheath, in the related discussion of Section 4.2, firstly, the advective type of self-coagulation that causes blue sheath is introduced. It is noticed that the comet-shaped coagulated structure is utilized to illustrate the advective self-coagulation, but it also applies to the semi-circle-shaped coagulated structure. Secondly, the ambipolar type of self-coagulation is introduced to explain the electrically neutral plasma core surrounded by a blue sheath. Similarly, the semi-circle-shaped coagulated structure is utilized to illustrate the ambipolar self-coagulation, but it also applies to the comet-shaped coagulated structure. Moreover, at the high electronegativity of Ar/SF<sub>6</sub> plasma, the decoupling of electron dynamics from the ambipolar self-coagulation of anion and cation pairs is also mentioned. In addition, in the process of introducing the ambipolar type of self-coagulation, the physical coagulation of anions that is driven by potential barrel and the chemical coagulation of anions that is self-happened by the chemistry are compared in the Ar/SF<sub>6</sub> plasma. It is seen from the simulation that the physical coagulation creates a cliffy border of anion density beneath the coil while the chemical coagulation creates a soft border of anion density therein, which implies the external physical factor is more robust than the internal chemical factor at coagulating the plasma anions.

In the Ar/SF<sub>6</sub> plasma, given by the ambipolar self-coagulation, each anion and cation species generated through discharge can have their respective coagulated structures. In Section 3.3, the third simulated phenomenon is given, i.e., the collapse of individual semi-circle-shaped coagulated structure. Concretely, for the anions, the coagulated peak of the sum of heavy SF<sub>5</sub><sup>-</sup> and SF<sub>6</sub><sup>-</sup> densities is dispersed by the light and coagulated F<sup>-</sup>. For the cations, the coagulated peak of heavy SF<sub>3</sub><sup>+</sup> is collapsed by the light and coagulated Ar<sup>+</sup>. It is seen that the lighter the species is, the easier it self-coagulates and the more difficult its coagulation is dispersed, which is determined by the inertia effect of density quantity. In addition, the destruction of coagulated cations by the expelling effect is more severe than the anions because the cations are coagulated by the ambipolar self-coagulation, which represents the collective interaction of electronegative plasma. It is essentially the electrically abstracting force of anions that are coagulated to the cations and weaker than the chemical self-coagulation force. Moreover, the collapse of the SF<sub>3</sub><sup>+</sup> coagulated peak leads to the spatially dispersed positive charge cloud. It is seen that the net charge cannot be shielded into a Debye's length, which implies the anti-collective behavior of plasma when they are self-coagulated into mass points, as modeled. In the related discussion of Section 4.3, the electrically expelling effect between individual coagulated structures with the same charge type is observed, and it is found that the Coulomb's force between the two point-charge models is maximal when the charge amounts that the models carry are equal. This truth explains well the disperse of coagulated SF<sub>5</sub><sup>-</sup> and SF<sub>6</sub><sup>-</sup> anions (the sum of them equates to the same density as F<sup>-</sup>) and the collapse of coagulated SF<sub>3</sub><sup>+</sup> cation (it has the same density as Ar<sup>+</sup>).

In Section 3.4, the fourth simulated phenomenon is given, i.e., rebuilding of coagulated structure by the Ar/SF<sub>6</sub> plasma species that have low densities, minor species such as F<sup>+</sup> and S<sup>+</sup>. It is seen from the simulation that, besides the main peak under the coil, these minor species are still coagulated along the discharge symmetrical axis, hence forming the second density peaks. The simulation shows that the net chemical sources of F<sup>+</sup> and S<sup>+</sup> at the locations of second density peaks are also negative. Together with the free diffusion therein (the ambipolar potential barrel is located around the main coagulated structure), the monopolar (pure positive) and spontaneous type of self-coagulation is suggested, which is not pre-pushed by ambipolar potential. Correspondingly, in the related discussion of

Section 4.4, the formula for the monopolar and non-advective types of self-coagulation are presented. In addition, simulated electrons also have this type of self-coagulation (pure negative polarity) in the periphery of the main coagulated structure (far away from the coil), which is also presented in this section. Finally, in Section 5, the conclusion and further remarks are given.

## 2. Fluid Model, Plasma Chemistry, and Reactor Configuration

### 2.1. Fluid Model Formulae

The formulae of the fluid model used in the work are described in this section. They include the mass, momentum, and energy equations of different plasma species, as well as the Poisson's and Maxwell's equations.

#### 2.1.1. Electrons Equation

The equations of electron density and energy are given as follows:

$$\begin{aligned}\frac{\partial n_e}{\partial t} + \nabla \cdot \mathbf{\Gamma}_e &= R_e, \\ \frac{\partial n_\varepsilon}{\partial t} + \nabla \cdot \mathbf{\Gamma}_\varepsilon + \mathbf{E} \cdot \mathbf{\Gamma}_e &= R_\varepsilon + P_{ohm}.\end{aligned}\quad (1)$$

The vectoral fluxes of electron density and energy at the assumption of drift and diffusion are described in Equation (2).

$$\begin{aligned}\mathbf{\Gamma}_e &= -\mu_e n_e \mathbf{E} - D_e \nabla n_e, \\ \mathbf{\Gamma}_\varepsilon &= -\mu_\varepsilon n_\varepsilon \mathbf{E} - D_\varepsilon \nabla n_\varepsilon.\end{aligned}\quad (2)$$

Herein,  $n_e$  and  $n_\varepsilon$  are the number density and energy density of electrons, respectively. Herein,  $n_e = \frac{3}{2} n_e k_B T_e$ .  $k_B$  is the Boltzmann's constant and  $T_e$  is the electron temperature in a unit of Kelvin.  $\mu_e$  and  $\mu_\varepsilon$  are the electron mobility and electron energy mobility, respectively.  $D_e$  and  $D_\varepsilon$  are electron diffusivity and electron energy diffusivity, respectively. The relations among the above mass and energy transport coefficients are  $D_e = \mu_e T_e$ ,  $D_\varepsilon = \mu_\varepsilon T_e$ , and  $\mu_\varepsilon = \frac{5}{3} \mu_e$ .  $\mathbf{E}$  is the vectoral and electrostatic field intensity caused by the ambi-polar diffusion and sheath.

$R_e$  and  $R_\varepsilon$  in Equation (1) are the respective source terms of number density and energy density of electrons. Their expressions are stated in Equation (3).

$$\begin{aligned}R_e &= \sum_{j=1}^M l_j k_j \prod_{m=1}^P n_m^{\nu_{jm}}, \\ R_\varepsilon &= \sum_{j=1}^M \varepsilon_j l_j k_j \prod_{m=1}^P n_m^{\nu_{jm}}.\end{aligned}\quad (3)$$

Herein,  $l_j$  is the number of electrons created (lost) per electron-impact reaction that generates (depletes) electrons.  $M$  is the number of these reactions.  $k_j$  is the rate coefficient of reaction  $j$ , which is expressed in the Sections 2.2 and 2.3 for the Ar/SF<sub>6</sub> and Ar/O<sub>2</sub> plasmas, respectively.  $n_m$  is the number density of reactant  $m$  of reaction  $j$ .  $\nu$  is the stoichiometric coefficient of the reaction and  $P$  is the number of reactants.  $\varepsilon_j$  is the electron energy loss per electron-impact reaction.

$P_{ohm}$  is the deposited power density via the Ohm's heating scheme, illustrated in Equation (4).

$$P_{ohm} = \frac{1}{2} \text{Re}(\sigma |E_\theta|^2).\quad (4)$$

Herein,  $\sigma$  is the electron conductivity.  $E_\theta$  is the radio frequency azimuthal field, which is calculated from Maxwell's equation; see next the Section 2.1.3. Without the secondary electron emissions, the boundary conditions for the above equations are set in Equation (5).

$$\begin{aligned} \mathbf{n} \cdot \Gamma_e &= \frac{1-r_e}{1+r} \left( \frac{1}{2} v_{e,th} n_e \right), \\ \mathbf{n} \cdot \Gamma_\varepsilon &= \frac{1-r_e}{1+r_e} \left( \frac{5}{6} v_{e,th} n_e \right). \end{aligned} \tag{5}$$

Herein,  $v_{e,th}$  is the thermal velocity of electrons.  $r_e$  is the reflection coefficient of electrons from the reactor wall, which is set to 0.2 in this model.

### 2.1.2. Heavy Species Equation

Heavy species are supposed to comprise a reacting flow that consists of  $k = 1, 2, \dots, Q$  species, except for the electron. The mass transport equations of these heavy species are summarized in Equation (6).

$$\rho \frac{\partial w_k}{\partial t} = \nabla \cdot \mathbf{j}_k + R_k. \tag{6}$$

Herein,  $\rho$  is the total mass density of heavy species and  $w_k$  is the mass fraction of species  $k$ .  $\mathbf{j}_k$  is the vectoral diffusive and drift flux of species  $k$  and expressed in Equation (7).

$$\begin{aligned} \mathbf{j}_k &= \rho w_k \mathbf{V}_k, \\ \mathbf{V}_k &= D_{k,m} \nabla \ln(w_k) - z_k \mu_m \mathbf{E}. \end{aligned} \tag{7}$$

Herein,  $\mathbf{V}_k$  is the vectoral velocity of species  $k$ ,  $z_k$  is elementary charge number that species  $k$  carries,  $\mu_m$  is the mobility, and  $\mathbf{E}$  is the electrostatic field vector, calculated from the Poisson's equation (see the Section 2.1.4). It is noted that the multi-component mass diffusion is considered and  $D_{k,m}$  is the averaged diffusion coefficient of mixture, expressed in Equation (8).

$$D_{k,m} = \frac{1 - w_k}{\sum_{j \neq k} x_j / D_{kj}}. \tag{8}$$

Herein,  $x_j$  is the number fraction of species  $j$  and  $D_{k,j}$  is the Chapman–Enskog binary diffusion coefficient [22,23].

The source term of Equation (6),  $R_k$ , is expressed in Equation (9).

$$R_k = M_k \sum_{j=1}^N l_{k,j} r_j. \tag{9}$$

Herein,  $M_k$  is the molecular weight,  $r_j$  is the rate of reaction  $j$  that creates or consumes species  $k$ ,  $N$  is the reaction number, and  $l_{k,j}$  is the particle number of species  $k$  created or consumed for each reaction  $j$ . The reaction rate,  $r_j$ , is expressed in Equation (10).

$$r_j = k_j \prod_{m=1}^S c_m^{v_{jm}}. \tag{10}$$

Herein,  $k_j$  is the rate coefficient, also given in Sections 2.2 and 2.3 for the Ar/SF<sub>6</sub> and Ar/O<sub>2</sub> plasmas, respectively.  $S$  is the number of reactants and  $v_{jm}$  is the stoichiometric coefficient of reaction  $j$  with arbitrary reactant  $m$  and the target reactant species  $k$ .  $c_m$  is the molar concentration of reactant  $m$ .

In sum, the heavy species equation of Equation (6) sequentially describes the inertia term, diffusion, drift, and chemical kinetics of heavy species. It is noted the inertia term considered herein is the inertia of mass, like the electron equation of Equation (1) (not the flux inertia) which we believe is one possible origin of self-coagulation happened in electronegative plasmas, i.e., the inertial effect of density quantity (see next the Section 4.3). In addition, only Q-2 equations are used since the mass fractions of feedstock gases of mixture, Ar and SF<sub>6</sub> (or Ar and O<sub>2</sub>), are governed by the mass constraint condition,  $\omega_{Ar,SF_6} = 1 - \sum_k^{Q-2} \omega_k$ , and the gas ratio between them assigned.

The total mass density of heavy species,  $\rho$ , is obtained from the ideal gas law in Equation (11).

$$\rho = \frac{P}{kT} \cdot \frac{M}{N_A}. \quad (11)$$

Herein,  $k$  is the Boltzmann's constant,  $T$  is gas temperature, equal to 300 K,  $P$  is the fixed gas pressure in a range of 10 mTorr to 90 mTorr as considered, and  $N_A$  is the Avogadro's constant.  $M$  is the mole averaged molecular weight, expressed in Equation (12).

$$\frac{1}{M} = \sum_{k=1}^Q \frac{w_k}{M_k}. \quad (12)$$

In general, the mean molecular weight of Equation (12),  $M$ , is not a constant, since it is a function of the mass fractions,  $w_k$ , and molecular weights of various species,  $M_k$ . The mass fractions that are calculated in Equation (6) are spatially and temporally varied.

The total flux boundary condition that includes the diffusion and drift components,  $\Gamma_k = -\mathbf{n} \cdot \rho \omega_k \mathbf{V}_{k,r}$ , is used on the chamber walls, where the surface kinetics of certain species that are listed in Tables 2 and 4 for the Ar/SF<sub>6</sub> and Ar/O<sub>2</sub> plasmas, respectively, are included.

### 2.1.3. Electromagnetic Equation

To describe the electromagnetic field in the reactor, Maxwell's equations are combined to express the Ampere's law in Equation (13).

$$(j\omega\sigma - \omega^2\varepsilon_0\varepsilon_r)\mathbf{A} + \nabla \times (\mu_0^{-1}\mu_r^{-1}\nabla \times \mathbf{A}) = \mathbf{J}_a. \quad (13)$$

Herein,  $j$  is the imaginary unit and  $\omega$  is the angular frequency of power source, expressed as  $2\pi f$  at  $f = 13.56\text{MHz}$ .  $\varepsilon_0$  and  $\varepsilon_r$  are the vacuum permittivity and the relative permittivity of dielectric window material (quartz), respectively.  $\mu_0$  and  $\mu_r$  are the vacuum permeability and the relative permeability of coil that is made of copper, respectively.  $\mathbf{A}$  is the magnetic vector potential, from which both the radio frequency (RF) magnetic and electric fields are calculated via the Coulomb's gauge, i.e.,  $\mathbf{B} = \nabla \times \mathbf{A}$ ,  $\mathbf{E} = -\frac{\partial \mathbf{A}}{\partial t}$ .  $\mathbf{J}_a$  is the current density of coil applied and will be persistently varied in the simulation until the deposited total power approaches the assigned value, i.e., 300 W. When considering the azimuthal symmetry, only the azimuthal component of RF electric field,  $E_\theta$ , and the axial and radial components of RF magnetic field,  $B_r, B_z$ , need to be addressed.  $\sigma$  is the electron conductivity, expressed in Equation (14). It is given by analytically solving the Langevin's equation at the assumption of zero electron temperature (~cold plasma), i.e., neglecting the diffusion [24].

$$\sigma = \frac{n_e q^2}{m_e (v_e + j\omega)}. \quad (14)$$

Herein,  $n_e$ ,  $m_e$ , and  $q$  are the number density, mass, and charge of electron, separately.  $v_e$  is the elastic collision frequency of electrons with the neutral species. The magnetic insulation, i.e.,  $\mathbf{n} \times \mathbf{A} = 0$ , is taken as the boundary condition for solving Maxwell's equation.

### 2.1.4. Electrostatic Equation

Poisson's equation is used to calculate electrostatic field in Equation (15).

$$\begin{aligned} \mathbf{E} &= -\nabla V, \\ \nabla \cdot \mathbf{D} &= \rho_V. \end{aligned} \quad (15)$$

Herein,  $\mathbf{E}$  is the electrostatic field,  $V$  is the potential, and  $\rho_V$  is the charge density of space, separately. Poisson's equation is only solved in the discharge chamber, and a zero potential boundary condition is used at both the chamber wall and the dielectric window downward surface. Our previous simulation of pure argon inductive discharge revealed

the approximation of grounded dielectric window potential does not significantly change the simulation results, and the reasonability of this approximation is extended to the present article. As mentioned before, only the axial and radial electrostatic field components are considered at the assumption of azimuthal symmetry. In sum, the mentioned electrons equation, heavy species equation, electromagnetic equation, and electrostatic equation are coupled together, and they are then numerically solved by the finite element method [25,26].

## 2.2. Chemistry of Ar/SF<sub>6</sub> Plasma

The Ar/SF<sub>6</sub> gas-phase chemistry and surface kinetics are given in Tables 1 and 2, respectively. The electron-impact elastic collision, excitation and de-excitation, ionization, direct attachment and dissociative attachment, and dissociation are included. The heavy species reaction types considered are neutral and ionic recombination, detachment, Penning ionization and charge exchange. The rate coefficients and cross sections of these reactions are taken from the Refs. [27–30]. The surface kinetics of species considered in Table 2 include recombination and de-excitation.

**Table 1.** Ar/SF<sub>6</sub> chemical reaction set considered in the model.

No.	Reaction	Rate Coefficient <sup>a</sup>	Threshold (eV)	Ref.
<u>Elastic collisions</u>				
1	$e + \text{Ar} \rightarrow e + \text{Ar}$	Cross section	0	[27]
2	$e + \text{SF}_6 \rightarrow e + \text{SF}_6$	Cross section	0	[27]
3	$e + \text{F}_2 \rightarrow e + \text{F}_2$	Cross section	0	[27]
4	$e + \text{F} \rightarrow e + \text{F}$	Cross section	0	[27]
<u>Excitation and de-excitation reactions</u>				
5	$e + \text{Ar} \rightarrow e + \text{Ar}^*$	Cross section	11.6	[27]
6	$e + \text{Ar}^* \rightarrow e + \text{Ar}$	Cross section	−11.6	[27]
<u>Ionization reactions</u>				
7	$e + \text{Ar} \rightarrow 2e + \text{Ar}^+$	Cross section	15.76	[27]
8	$e + \text{Ar}^s \rightarrow 2e + \text{Ar}^+$	Cross section	4.43	[27]
9	$e + \text{SF}_6 \rightarrow \text{SF}_5^+ + \text{F} + 2e$	$1.2 \times 10^{-7} \exp(-18.1/T_e)$	16	[28,29]
10	$e + \text{SF}_6 \rightarrow \text{SF}_4^+ + 2\text{F} + 2e$	$8.4 \times 10^{-9} \exp(-19.9/T_e)$	20	[28,29]
11	$e + \text{SF}_6 \rightarrow \text{SF}_3^+ + 3\text{F} + 2e$	$3.2 \times 10^{-8} \exp(-20.7/T_e)$	20.5	[28,29]
12	$e + \text{SF}_6 \rightarrow \text{SF}_2^+ + \text{F}_2 + 2\text{F} + 2e$	$7.6 \times 10^{-9} \exp(-24.4/T_e)$	28	[28,29]
13	$e + \text{SF}_6 \rightarrow \text{SF}^+ + \text{F}_2 + 3\text{F} + 2e$	$1.2 \times 10^{-8} \exp(-26.0/T_e)$	37.5	[28,29]
14	$e + \text{SF}_6 \rightarrow \text{F}^+ + \text{SF}_4 + \text{F} + 2e$	$1.2 \times 10^{-8} \exp(-31.7/T_e)$	29	[28,29]
15	$e + \text{SF}_6 \rightarrow \text{S}^+ + 4\text{F} + \text{F}_2 + 2e$	$1.4 \times 10^{-8} \exp(-39.9/T_e)$	18	[28,29]
16	$e + \text{SF}_5 \rightarrow \text{SF}_5^+ + 2e$	$1.0 \times 10^{-7} \exp(-17.8/T_e)$	11	[28,29]
17	$e + \text{SF}_5 \rightarrow \text{SF}_4^+ + \text{F} + 2e$	$9.4 \times 10^{-8} \exp(-22.8/T_e)$	15	[28,29]
18	$e + \text{SF}_4 \rightarrow \text{SF}_4^+ + 2e$	$4.77 \times 10^{-8} \exp(-16.35/T_e)$	13	[28,29]
19	$e + \text{SF}_4 \rightarrow \text{SF}_3^+ + \text{F} + 2e$	$5.31 \times 10^{-8} \exp(-17.67/T_e)$	14.5	[28,29]
20	$e + \text{SF}_3 \rightarrow \text{SF}_3^+ + 2e$	$1.0 \times 10^{-7} \exp(-18.9/T_e)$	11	[28,29]
21	$e + \text{F} \rightarrow \text{F}^+ + 2e$	$1.3 \times 10^{-8} \exp(-16.5/T_e)$	15	[28,29]
22	$e + \text{S} \rightarrow \text{S}^+ + 2e$	$1.6 \times 10^{-7} \exp(-13.3/T_e)$	10	[28,29]
23	$e + \text{F}_2 \rightarrow \text{F}_2^+ + 2e$	$1.37 \times 10^{-8} \exp(-20.7/T_e)$	15.69	[28,29]
<u>Attachment and dissociative attachment reactions</u>				
24	$e + \text{SF}_6 \rightarrow \text{SF}_6^-$	Cross section	0	[27]
25	$e + \text{SF}_6 \rightarrow \text{SF}_5^- + \text{F}$	Cross section	0.1	[27]
26	$e + \text{SF}_6 \rightarrow \text{SF}_4^- + 2\text{F}$	Cross section	5.4	[27]
27	$e + \text{SF}_6 \rightarrow \text{SF}_3^- + 3\text{F}$	Cross section	11.2	[27]
28	$e + \text{SF}_6 \rightarrow \text{SF}_2^- + 4\text{F}$	Cross section	12	[27]
29	$e + \text{SF}_6 \rightarrow \text{F}^- + \text{SF}_5$	Cross section	2.9	[27]
30	$e + \text{SF}_6 \rightarrow \text{F}_2^- + \text{SF}_4$	Cross section	5.4	[27]
31	$e + \text{F}_2 \rightarrow \text{F}^- + \text{F}$	Cross section	0	[27]

Table 1. Cont.

No.	Reaction	Rate Coefficient <sup>a</sup>	Threshold (eV)	Ref.
<u>Dissociation reactions</u>				
32	$e + SF_6 \rightarrow SF_5 + F + e$	$1.5 \times 10^{-7} \exp(-8.1/T_e)$	9.6	[28,29]
33	$e + SF_6 \rightarrow SF_4 + 2F + e$	$9.0 \times 10^{-9} \exp(-13.4/T_e)$	12.4	[28,29]
34	$e + SF_6 \rightarrow SF_3 + 3F + e$	$2.5 \times 10^{-8} \exp(-33.5/T_e)$	16	[28,29]
35	$e + SF_6 \rightarrow SF_2 + F_2 + 2F + e$	$2.3 \times 10^{-8} \exp(-33.9/T_e)$	18.6	[28,29]
36	$e + SF_6 \rightarrow SF + F_2 + 3F + e$	$1.5 \times 10^{-9} \exp(-26.0/T_e)$	22.7	[28,29]
37	$e + SF_5 \rightarrow SF_4 + F + e$	$1.5 \times 10^{-7} \exp(-9.0/T_e)$	5	[28,29]
38	$e + SF_4 \rightarrow SF_3 + F + e$	$6.2 \times 10^{-8} \exp(-9.0/T_e)$	8.5	[28,29]
39	$e + SF_3 \rightarrow SF_2 + F + e$	$8.6 \times 10^{-8} \exp(-9.0/T_e)$	5	[28,29]
40	$e + SF_2 \rightarrow SF + F + e$	$4.5 \times 10^{-8} \exp(-9.0/T_e)$	8	[28,29]
41	$e + SF \rightarrow S + F + e$	$6.2 \times 10^{-8} \exp(-9.0/T_e)$	7.9	[28,29]
42	$e + F_2 \rightarrow 2F + e$	$1.2 \times 10^{-8} \exp(-5.8/T_e)$	1.6	[28,29]
<u>Neutral/neutral recombination reactions</u>				
43	$S + F \rightarrow SF$	$2 \times 10^{-16}$	0	[28,29]
44	$SF + F \rightarrow SF_2$	$2.9 \times 10^{-14}$	0	[28,29]
45	$SF_2 + F \rightarrow SF_3$	$2.6 \times 10^{-12}$	0	[28,29]
46	$SF_3 + F \rightarrow SF_4$	$1.6 \times 10^{-11}$	0	[28,29]
47	$SF_4 + F \rightarrow SF_5$	$1.7 \times 10^{-11}$	0	[28,29]
48	$SF_5 + F \rightarrow SF_6$	$1.0 \times 10^{-11}$	0	[28,29]
49	$SF_3 + SF_3 \rightarrow SF_2 + SF_4$	$2.5 \times 10^{-11}$	0	[28,29]
50	$SF_5 + SF_5 \rightarrow SF_4 + SF_6$	$2.5 \times 10^{-11}$	0	[28,29]
51	$SF + SF \rightarrow S + SF_2$	$2.5 \times 10^{-11}$	0	[28,29]
52	$SF_x + F_2 \rightarrow SF_{x+1} + F$ <sup>b</sup>	$7.0 \times 10^{-15}$	0	[28,29]
<u>Ion/ion recombination reactions</u>				
53	$X^+ + Y^- \rightarrow X + Y$ <sup>c</sup>	$5.0 \times 10^{-9}$	0	[28,29]
<u>Detachment reactions</u>				
54	$Z + Y^- \rightarrow Z + Y + e$ <sup>d</sup>	$5.27 \times 10^{-14}$	0	[28,29]
<u>Other reactions</u>				
55	$Ars + Ars \rightarrow e + Ar + Ar^+$	$6.2 \times 10^{-10}$	0	[28,29]
56	$Ars + Ar \rightarrow Ar + Ar$	$3.0 \times 10^{-15}$	0	[28,29]
57	$Ar^+ + SF_6 \rightarrow SF_5^+ + F + Ar$	$9.0 \times 10^{-10}$	0	[28,29]
58	$SF_5^+ + SF_6 \rightarrow SF_3^+ + SF_6 + F_2$	$6.0 \times 10^{-12}$	0	[28,29]

<sup>a</sup> The unit of the rate coefficient is  $cm^3 s^{-1}$ . For certain collisions of electron impact, such as the elastic scattering, excitation and de-excitation, and the attachment, the cross sections are used. The rate coefficients of these reactions are calculated through the cross sections and assumed Maxwellian-type of electron energy distribution function, as expressed by the following formula:  $k(r, z) = \int_0^\infty f(r, z, \epsilon) \times \left(\frac{2\epsilon}{m}\right)^{1/2} \sigma(\epsilon) d\epsilon$ . Herein,  $k(r, z)$  is the rate coefficient of two-dimensional space,  $f(r, z, \epsilon)$  is the assumed electron energy distribution function,  $\epsilon$  is the translational energy of electrons,  $m$  is the electron mass, and  $\sigma(\epsilon)$  is the related cross section. <sup>b</sup>  $x$  stands for the number 1–5. <sup>c</sup>  $X = SF_5, SF_4, SF_3, SF_2, SF, F, S$ , or  $F_2$ ;  $Y = SF_6, SF_5, SF_4, SF_3, SF_2, F$ , or  $F_2$ ; <sup>d</sup>  $Z = SF_6, SF_5, SF_4, SF_3, SF_2, SF, F, S$ , or  $F_2$ ;  $Y = SF_6, SF_5, SF_4, SF_3, SF_2, F$ , or  $F_2$ .

Table 2. Ar/SF<sub>6</sub> surface reaction set considered in the model.

No.	Surface Reaction	Sticking Coefficient	Ref.
1	$SF_x^+ + wall \rightarrow SF_x$ ; $x = 1 - 5$	1	[28,29]
2	$F^+ + wall \rightarrow F$	1	[28,29]
3	$F_2^+ + wall \rightarrow F_2$	1	[28,29]
4	$S^+ + wall \rightarrow S$	1	[28,29]
5	$F + wall \rightarrow 1/2F_2$	0.02	[30]
6	$Ar^+ + wall \rightarrow Ar$	1	[28,29]
7	$Ars + wall \rightarrow Ar$	1	[28,29]

### 2.3. Chemistry of Ar/O<sub>2</sub> Plasma and O<sup>-</sup> Chemical Kinetics

As listed in Table 3, the gas phase chemistry of the Ar/O<sub>2</sub> plasma fluid simulation considers (1) elastic, ionization, dissociative attachment, electronic excitation, de-excitation, and detachment between the electrons and neutral species, and (2) metastable quenching,

recombination, associative detachment, and charge transfer between the heavy species. In total, the chemical set contains five charged species, i.e., electron,  $O^-$ ,  $O^+$ ,  $O_2^+$ , and  $Ar^+$ ; three metastable molecules, i.e.,  $O_2^*$ ,  $O^*$ , and  $Ar^*$ ; and three grounded molecules, i.e.,  $O$ ,  $Ar$ , and  $O_2$ . The surface reactions of reactive species are listed in Table 4. The rate coefficients and cross sections of these reactions, as well as the surface kinetics, are taken from the Refs. [31–38]. Specially, the reactions for the  $O^-$  generation and loss are collected in Tables 5 and 6, respectively, for the convenience of observing  $O^-$  chemical kinetics (see the results and discussion parts). In the chemical kinetics of  $O^-$ , reaction No. 3 mainly contributes to the  $O^-$  generation, and reaction No. 42 mainly contributes to the  $O^-$  loss.

#### 2.4. ICP Reactor Configuration

The ICP reactor used consists of the vacuum chamber (also called matching box) and the discharge chamber, which are separated by the dielectric window. The discharge chamber is 15 cm in radius and 13 cm in height. The dielectric window and vacuum chamber hold the same radius as the discharge chamber and the heights of them are 1 cm and 3 cm, respectively. A substrate with a radius of 12 cm and a height of 4 cm is seated at the bottom center of discharge chamber. A two-turn coil is installed above the dielectric window, with radial locations of 8 cm and 10 cm, respectively. The coil is square in cross section, with a side length of 0.6 cm. More details on the ICP reactor can be found in Ref. [39] and Figure 1.

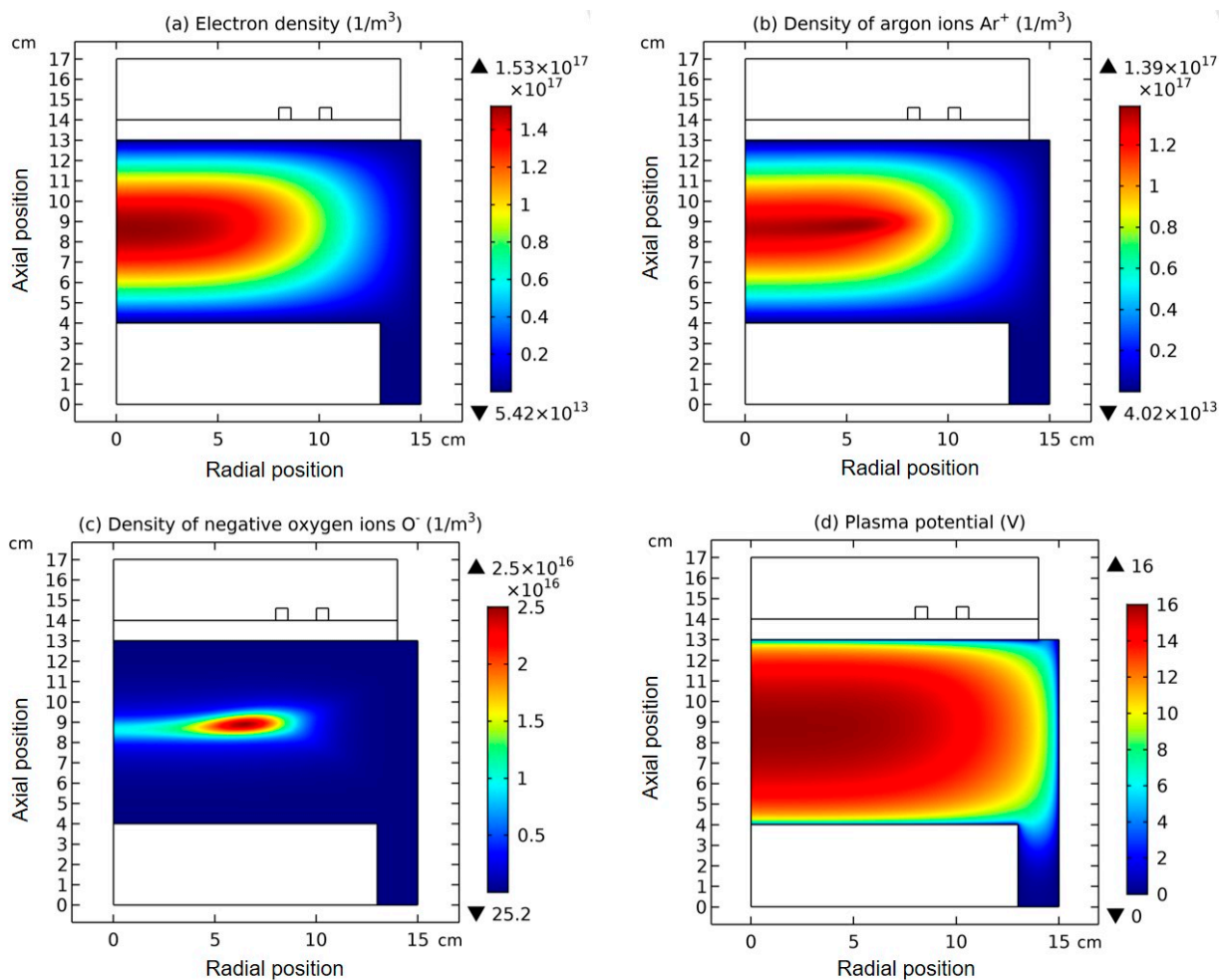


**Figure 1.** Simulated two-dimensional profiles of (a) electron density, (b)  $Ar^+$  density, (c)  $O^-$  density, and (d) plasma potential in  $Ar/O_2$  plasma, by means of fluid model and at the discharge conditions of 300 W, 30 mTorr, and 10%  $O_2$  content.

**Table 3.** Chemical reactions for Ar/O<sub>2</sub> discharges included in the fluid model.

No.	Reaction	Rate Coefficient (cm <sup>3</sup> /s) <sup>a</sup>	Threshold (eV)	References
1	e + O <sub>2</sub> → e + O <sub>2</sub>	4.7 × 10 <sup>-8</sup> T <sub>e</sub> <sup>0.5</sup>	3T <sub>e</sub> (m <sub>e</sub> /m <sub>n</sub> )	[31]
2	e + O <sub>2</sub> → 2e + O <sub>2</sub> <sup>+</sup>	9.0 × 10 <sup>-10</sup> T <sub>e</sub> <sup>0.5</sup> exp(-12.6/T <sub>e</sub> )	12.06	[31]
3	e + O <sub>2</sub> → O <sup>-</sup> + O	8.8 × 10 <sup>-11</sup> exp(-4.4/T <sub>e</sub> )	3.637	[32]
4	e + O <sub>2</sub> → e + O <sup>-</sup> + O <sup>+</sup>	7.1 × 10 <sup>-11</sup> T <sub>e</sub> <sup>0.5</sup> exp(-17.0/T <sub>e</sub> )	17	[31]
5	e + O <sub>2</sub> → 2e + O + O <sup>+</sup>	5.3 × 10 <sup>-10</sup> T <sub>e</sub> <sup>0.9</sup> exp(-20.0/T <sub>e</sub> )	20	[32]
6	e + O <sub>2</sub> → e + O <sub>2</sub> <sup>*</sup>	1.7 × 10 <sup>-9</sup> exp(-3.1/T <sub>e</sub> )	0.98	[31]
7 <sup>b</sup>	e + O <sub>2</sub> → e + O <sup>*</sup> + O	5.0 × 10 <sup>-8</sup> exp(-8.4/T <sub>e</sub> )	8.57	[32]
8	e + O <sub>2</sub> → e + 2O	4.2 × 10 <sup>-9</sup> exp(-4.4/T <sub>e</sub> )	6.4	[32]
9	e + O → 2e + O <sup>+</sup>	9.0 × 10 <sup>-9</sup> T <sub>e</sub> <sup>0.7</sup> exp(-13.0/T <sub>e</sub> )	13	[32]
10	e + O → e + O <sup>*</sup>	4.2 × 10 <sup>-9</sup> exp(-2.25/T <sub>e</sub> )	1.97	[32]
11 <sup>b</sup>	e + O <sup>*</sup> → e + O	8.0 × 10 <sup>-9</sup>	-1.97	[32]
12 <sup>b</sup>	e + O <sup>*</sup> → 2e + O <sup>+</sup>	9.0 × 10 <sup>-9</sup> T <sub>e</sub> <sup>0.7</sup> exp(-11.6/T <sub>e</sub> )	11.6	[32]
13	e + O <sup>-</sup> → 2e + O	2.0 × 10 <sup>-7</sup> exp(-5.5/T <sub>e</sub> )	5.5	[32]
14	e + O <sub>2</sub> <sup>+</sup> → 2O	5.2 × 10 <sup>-9</sup> /T <sub>e</sub>	-6.96	[32]
15 <sup>b</sup>	e + O <sub>2</sub> <sup>*</sup> → e + O <sub>2</sub>	5.6 × 10 <sup>-9</sup> exp(-2.2/T <sub>e</sub> )	-0.98	[31]
16 <sup>b</sup>	e + O <sub>2</sub> <sup>*</sup> → O <sup>-</sup> + O	2.28 × 10 <sup>-10</sup> exp(-2.29/T <sub>e</sub> )	5.19	[33]
17 <sup>b</sup>	e + O <sub>2</sub> <sup>*</sup> → 2e + O <sub>2</sub> <sup>+</sup>	9.0 × 10 <sup>-10</sup> T <sub>e</sub> <sup>2.0</sup> exp(-11.6/T <sub>e</sub> )	11.08	[32]
18 <sup>b</sup>	e + O <sub>2</sub> <sup>*</sup> → e + 2O	4.2 × 10 <sup>-9</sup> exp(-4.6/T <sub>e</sub> )	5.42	[32]
19 <sup>b</sup>	e + O <sub>2</sub> <sup>*</sup> → e + O <sup>*</sup> + O	2.04 × 10 <sup>-8</sup> exp(-7.4/T <sub>e</sub> )	7.59	[33]
20 <sup>b</sup>	e + O <sub>2</sub> <sup>*</sup> → 2e + O <sup>+</sup> + O	5.3 × 10 <sup>-10</sup> T <sub>e</sub> <sup>0.9</sup> exp(-19.0/T <sub>e</sub> )	17.7	[31]
21	e + Ar → e + Ar	Cross section <sup>c</sup>	15.6	[34]
22 <sup>b</sup>	e + Ar → e + Ar <sup>*</sup>	Cross section	11.50	[34]
23 <sup>b</sup>	e + Ar <sup>*</sup> → e + Ar	Cross section	-11.50	[34]
24	e + Ar → 2e + Ar <sup>+</sup>	Cross section	15.80	[34]
25 <sup>b</sup>	e + Ar <sup>*</sup> → 2e + Ar <sup>+</sup>	Cross section	4.427	[34]
26	O <sup>-</sup> + O <sub>2</sub> <sup>+</sup> → O + O <sub>2</sub>	1.0 × 10 <sup>-7</sup>		[33]
27	O <sup>-</sup> + O → e + O <sub>2</sub>	3.0 × 10 <sup>-10</sup>		[35]
28	O <sup>-</sup> + O <sup>+</sup> → 2O	2.7 × 10 <sup>-7</sup> (300.0/T <sub>n</sub> ) <sup>0.5</sup>		[33]
29	O <sup>-</sup> + O <sub>2</sub> <sup>+</sup> → 3O	1.0 × 10 <sup>-7</sup>		[33]
30	O <sup>+</sup> + O <sub>2</sub> → O + O <sub>2</sub> <sup>+</sup>	2.0 × 10 <sup>-11</sup> (300.0/T <sub>n</sub> ) <sup>0.5</sup>		[35]
31 <sup>b</sup>	O <sub>2</sub> <sup>*</sup> + O <sub>2</sub> → 2O <sub>2</sub>	2.2 × 10 <sup>-18</sup> (300.0/T <sub>n</sub> )		[33]
32 <sup>b</sup>	O <sub>2</sub> <sup>*</sup> + O → O <sub>2</sub> + O	2.0 × 10 <sup>-16</sup>		[33]
33 <sup>b</sup>	O <sup>*</sup> + O → 2O	8.0 × 10 <sup>-12</sup>		[35]
34 <sup>b</sup>	O <sup>*</sup> + O <sub>2</sub> → O + O <sub>2</sub> <sup>*</sup>	1.0 × 10 <sup>-12</sup>		[35]
35 <sup>b</sup>	O <sup>*</sup> + O <sub>2</sub> → O + O <sub>2</sub>	7.0 × 10 <sup>-12</sup> exp(67.0/T <sub>n</sub> )		[35]
36 <sup>b</sup>	O <sup>+</sup> + O <sub>2</sub> <sup>*</sup> → O + O <sub>2</sub> <sup>+</sup>	2.1 × 10 <sup>-11</sup>		[33]
37 <sup>b</sup>	O <sup>-</sup> + O <sub>2</sub> <sup>*</sup> → O + O <sub>2</sub> + e	1.0 × 10 <sup>-10</sup> (-100.0/T <sub>i</sub> ) <sup>0.5</sup>		[33]
38	O <sub>2</sub> + Ar <sup>+</sup> → O <sub>2</sub> <sup>+</sup> + Ar	1.1 × 10 <sup>-10</sup>		[36]
39	O <sub>2</sub> <sup>*</sup> + Ar <sup>+</sup> → O <sub>2</sub> <sup>+</sup> + Ar	1.1 × 10 <sup>-10</sup>		[36]
40	O + Ar <sup>+</sup> → O <sup>+</sup> + Ar	1.1 × 10 <sup>-10</sup>		[36]
41 <sup>b</sup>	O <sup>*</sup> + Ar <sup>+</sup> → O <sup>+</sup> + Ar	1.1 × 10 <sup>-10</sup>		[36]
42	O <sup>-</sup> + Ar <sup>+</sup> → O + Ar	2.8 × 10 <sup>-7</sup>		[33]
43	O <sub>2</sub> <sup>+</sup> + Ar → O <sub>2</sub> + Ar <sup>+</sup>	5.5 × 10 <sup>-11</sup>		[33]
44 <sup>b</sup>	O <sub>2</sub> + Ar <sup>*</sup> → O + O + Ar	2.4 × 10 <sup>-10</sup>		[37]

<sup>a</sup> T<sub>e</sub> is the electron temperature, in a unit of eV, and T<sub>n</sub>, and T<sub>i</sub> are the neutrals and ions temperature, both equal to 300 K. <sup>b</sup> The symbol \* in these reactions represents metastable species. <sup>c</sup> The reaction rate is calculated based on related cross section and the Maxwellian's electron energy distribution function (more detail of the process can be found in the footnote of Table 1).

**Table 4.** Surface reactions for Ar/O<sub>2</sub> discharges included in the fluid model.

No.	Surface Reactions	Reference
1	$O_2^+ + \text{wall} \rightarrow O_2$	[38]
2	$O^+ + \text{wall} \rightarrow O$	[38]
3	$O_2^* + \text{wall} \rightarrow O_2$	[38]
4	$O^* + \text{wall} \rightarrow O$	[38]
5	$O^- + \text{wall} \rightarrow O$	[38]
6	$O + \text{wall} \rightarrow 1/2O_2$	[38]
7	$O + \text{wall} \rightarrow 1/2O_2^*$	[38]
8	$Ar^+ + \text{wall} \rightarrow Ar$	[34]
9	$Ar^* + \text{wall} \rightarrow Ar$	[34]

**Table 5.** Reactions collection for O<sup>−</sup> generation.

No.	Reaction
3	$e + O_2 \rightarrow O^- + O$
4	$e + O_2 \rightarrow e + O^- + O^+$
16	$e + O_2^* \rightarrow O^- + O$

**Table 6.** Reactions collection for O<sup>−</sup> loss.

No.	Reaction
13	$e + O^- \rightarrow 2e + O$
26	$O^- + O_2^+ \rightarrow O + O_2$
27	$O^- + O \rightarrow e + O_2$
28	$O^- + O^+ \rightarrow 2O$
29	$O^- + O_2^+ \rightarrow 3O$
37	$O^- + O_2^* \rightarrow O + O_2 + e$
42	$O^- + Ar^+ \rightarrow O + Ar$

### 3. Results

In this section, the four simulated phenomena by fluid model are presented, i.e., comet-shaped coagulated structure in Ar/O<sub>2</sub> plasma (see Section 3.1), blue sheaths that surround the electrically neutral plasmas in both the Ar/O<sub>2</sub> plasma for comet-shaped structure and the Ar/SF<sub>6</sub> plasma for semi-circle-shaped structure (see Section 3.2), collapse or disperse of semi-circle-shaped structures of certain cations and anions in Ar/SF<sub>6</sub> plasma when they are presented individually and the spatially dispersed positive charge cloud created by the collapse of cation coagulation (see Section 3.3), and rebuilding of coagulated structure by minor species in Ar/SF<sub>6</sub> plasma at the discharge symmetrical axis (see Section 3.4). Herein, the characteristics of these phenomena are analyzed, and the underlined mechanisms of them will be given in Section 4.

#### 3.1. Comet Structure

The comet-shaped density profile of anions (O<sup>−</sup>) is found in the fluid simulation of Ar/O<sub>2</sub> plasma, as shown in Figure 1c. This novel density profile of plasma species provokes our profound interest since it has never been reported before. As seen, the comet-shaped O<sup>−</sup> density looks like a Dirac delta function, especially in the axial direction. To investigate the mechanism behind this, the relevant quantities are observed, such as the electron density, argon ion Ar<sup>+</sup> density, plasma potential in Figure 1, and its chemical processes, including the reaction rates of O<sup>−</sup> generation and loss and the summed rate shown in Figure 2. An important feature that the O<sup>−</sup> species have a negative chemical source in the located density peak is noticed. In the mature analytic works (see Ref. [1], pp. 330–333), the species density morphologies of electropositive plasma, such as the parabola, cosine, and Bessel at high pressure limit, the variable mobility model of intermediate pressure range, and the Langmuir solution at low pressure limit, are all based on the continuity equation of

species with positive chemical source. This is logical since in the electropositive plasmas the species are depleted on the chamber wall through surface kinetics. In the electronegative plasmas, this is not always true. In Figure 2, at certain circumstances (low electronegativity), the negative source of anions given by the recombination exceeds the positive source given by the electron-impact dissociative attachment. The chemical kinetics of  $O^-$  species can be referred to from Tables 5 and 6. The analysis above implies that when the chemical source is negative, it tends to create a coagulated structure in the electronegative plasma.

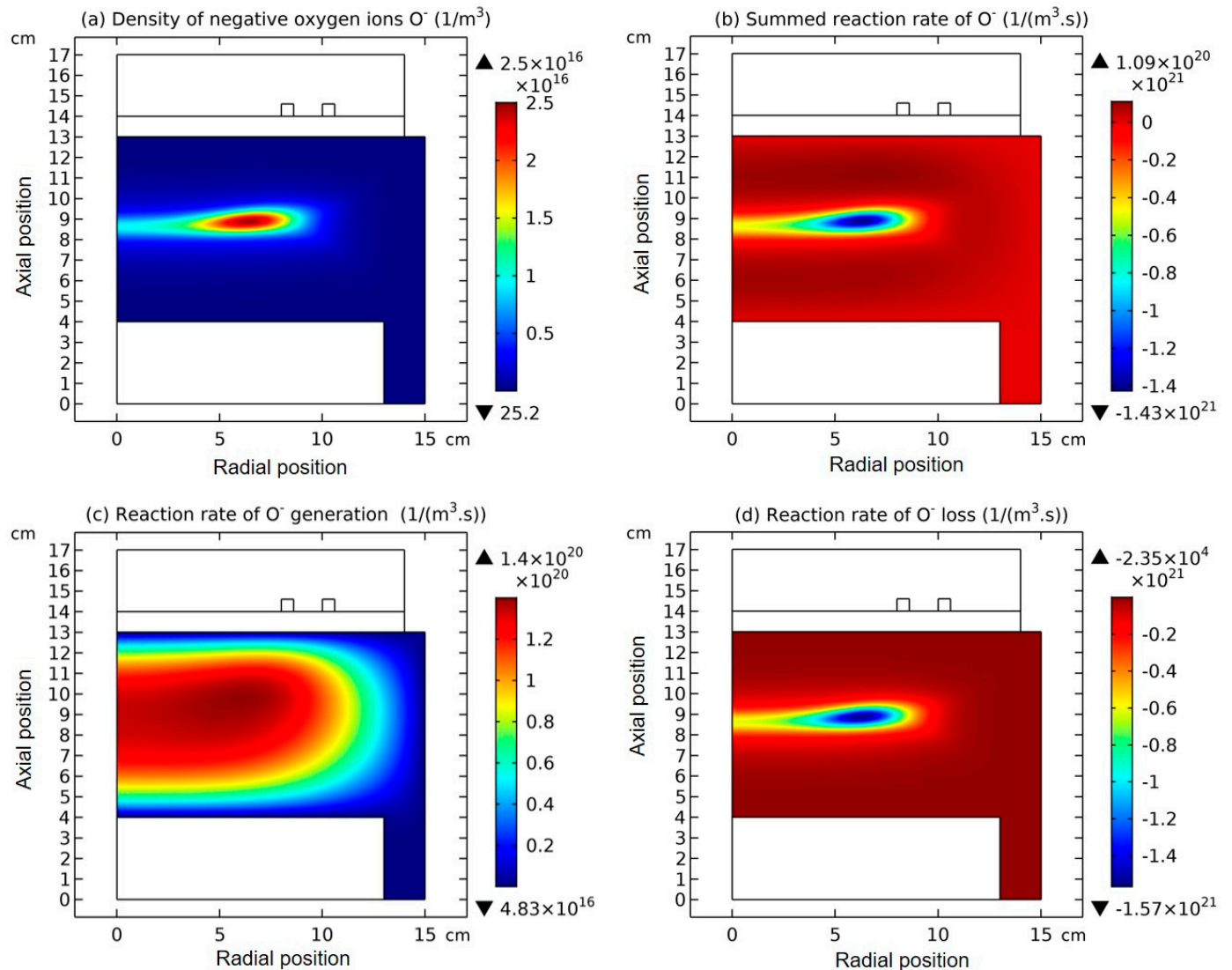


**Figure 2.** Simulated two-dimensional profiles of (a)  $O^-$  density, (b) summed reaction rate of  $O^-$ , (c) reaction rate for  $O^-$  generation, and (d) reaction rate for  $O^-$  loss in Ar/ $O_2$  plasma by means of fluid model and at the discharge conditions of 300 W, 30 mTorr, and 10%  $O_2$  content.

It is seen in Figure 1c,d that the delta type of  $O^-$  is located on the top of the ambipolar potential, and its main transport component is then free diffusion since the drift is negligible. To qualitatively interpret the forming mechanism of delta, the unsteady-state continuity equation of  $O^-$  that consists of the free diffusion flux and negative chemical source of recombination is presented in Equation (16). Herein,  $D_-$  is the diffusion coefficient of  $O^-$  and  $\nu_{rec}$  is the recombination frequency of it.  $n_-$  represents the  $O^-$  density. As seen next, through the dimension analysis, the negative chemical source can be transformed into drift flux that may be caused by an *effective* electric field. In Equation (17), the transformed drift

flux  $\vec{\Gamma}_d$  of the *effective* field and its divergence are given. Herein,  $\vec{E}$  is the *effective* field and  $\rho$  is the net charge density transformed. Note that in the process of calculating the divergence, the Poisson's equation is used. In addition, the dimensional analysis is executed only for the second term of flux divergence,  $\mu_- n_- \frac{\rho}{\epsilon_0}$ . The first term of divergence,  $\mu_- \nabla n_- \cdot \vec{E}$ , is not chosen for dimension analysis since it contains the density gradient, which does not exist at the condition of a delta density type. As seen in Equation (18), the dimension of  $\mu_- n_- \frac{\rho}{\epsilon_0}$  is the same as the chemical source,  $n_- v_{rec}$ . It is stressed herein that the dimensional analysis is not enough for validating the drift role of chemical source, but the fact that chemical source contains the density of species considered, herein  $n_-$ , representing the density of  $O^-$ , is a key factor for suggesting such a transformation. It is meant that the considered species is attracted by the transformed *potential* of recombination. This attraction is balanced by free diffusion, illustrated in Equations (19)–(21), and ultimately the delta type of  $O^-$  is formed. This is more of a static mechanic system, not a dynamic transport problem anymore. More detail of the supposed static balance is given in the self-coagulation theory (see Section 4.1).

$$\frac{\partial n_-}{\partial t} - D_- \nabla^2 n_- = -n_- v_{rec}, \quad (16)$$

$$\vec{\Gamma}_d = \mu_- n_- \vec{E}, \quad (17)$$

$$\nabla \cdot \vec{\Gamma}_d = \mu_- \nabla n_- \cdot \vec{E} + \mu_- n_- \nabla \cdot \vec{E} = \mu_- \nabla n_- \cdot \vec{E} + \mu_- n_- \frac{\rho}{\epsilon_0},$$

$$[\mu_-] = \frac{m^2}{V \cdot s}, [n_-] = \frac{1}{m^3}, [\rho] = \frac{C}{m^3}, [\epsilon_0] = \frac{C}{m \cdot V}, \quad (18)$$

$$[\mu_- n_- \frac{\rho}{\epsilon_0}] = \frac{1}{m^3 \cdot s} = [n_- v_{rec}],$$

$$\frac{\partial n_-}{\partial t} - D_- \nabla^2 n_- + n_- v_{rec} = 0, \quad (19)$$

$$\frac{\partial n_-}{\partial t} - D_- \nabla^2 n_- + \mu_- n_- \frac{\rho}{\epsilon_0} = 0, \quad (20)$$

$$\frac{\partial n_-}{\partial t} - D_- \nabla^2 n_- + \nabla \cdot \vec{\Gamma}_d = 0. \quad (21)$$

### 3.2. Blue Sheath Phenomenon

It is seen that around the comet in Ar/O<sub>2</sub> plasma of Figure 3a, there is a layer of “blue” sheath. The blue sheath is an electronegative sheath, among which the net charge density is negative (see the legend of Figure 3b for reference). Similarly, in the Ar/SF<sub>6</sub> plasma of Figure 4 with high electronegativity, around the semi-circle (another coagulated structure) there is a layer of blue sheath as well. As seen next in Section 4.2, the blue sheath is caused by the advective self-coagulation, and the internal electrically neutral plasma that is surrounded by the blue sheath is sustained by the ambipolar self-coagulation.

### 3.3. Collapse of Individual Semi-Circle Structure

Ar/SF<sub>6</sub> gaseous discharge creates many species of cation and anion (refer to the chemistry of Ar/SF<sub>6</sub> plasma in Section 2). In Sections 3.2 and 4.2, the densities of cations and anions are summed, respectively. In the present section, it is seen that the coagulated structures of certain species collapse when the densities of anions and cations are shown individually. In Figure 5a,b the density profiles of F<sup>−</sup> species at two selected simulating times, 10<sup>−4</sup>s and 1.0 s, are shown, and in Figure 5c–f the density profiles of SF<sub>6</sub><sup>−</sup> and SF<sub>5</sub><sup>−</sup> species of the two times are shown. As seen, when increasing the simulation time, the coagulated profile of F<sup>−</sup> is kept while the coagulations of SF<sub>6</sub><sup>−</sup> and SF<sub>5</sub><sup>−</sup> are obviously dispersed. Moreover, in the profiles of SF<sub>6</sub><sup>−</sup> and SF<sub>5</sub><sup>−</sup> the density vacancies appear at the precise positions where the F<sup>−</sup> species are coagulated. As seen in Section 4.3, the dispersions of these anion density profiles are caused by the electrically expelling force that

exist between themselves and their opponent,  $F^-$ , after they are viewed as mass-point (or more precisely, point-charge) models.

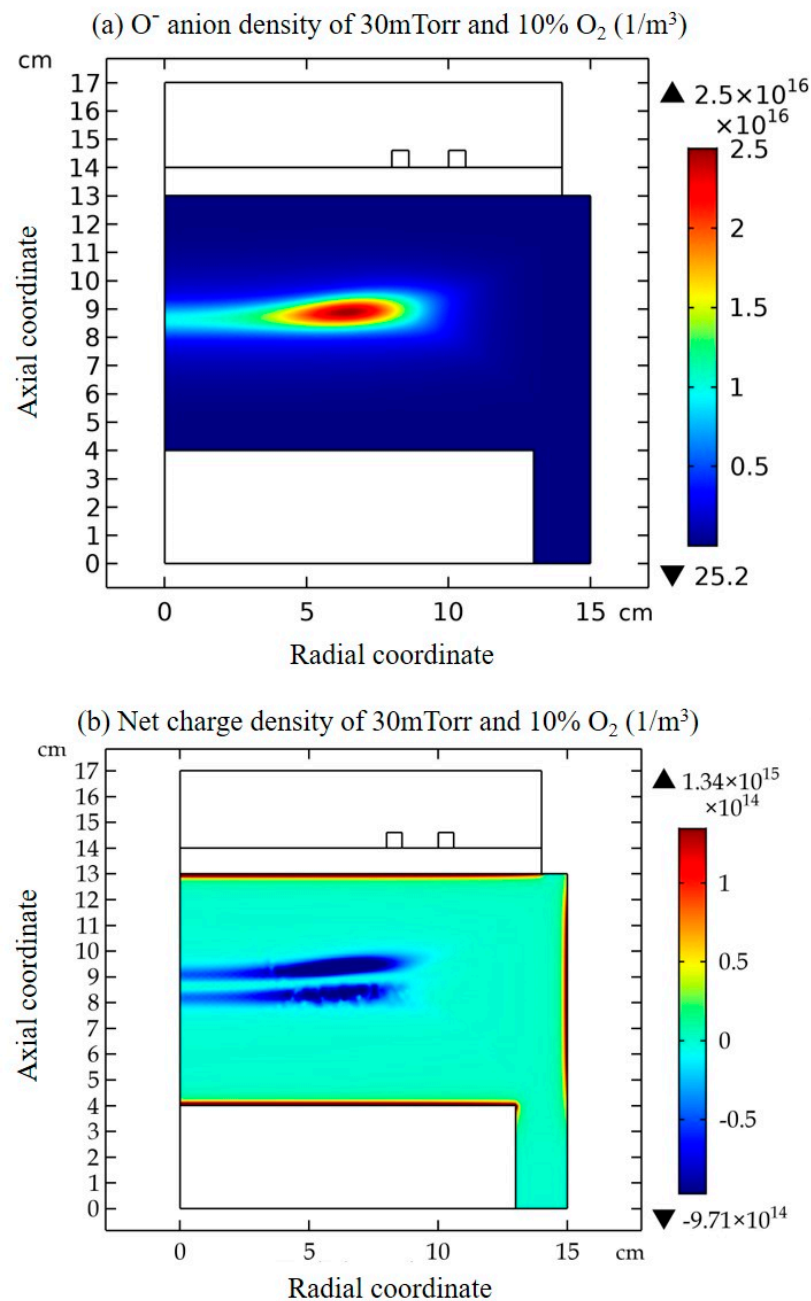


**Figure 3.** Simulated two-dimensional profiles of (a)  $O^-$  density and (b) net charge density in Ar/ $O_2$  plasma, by means of fluid model. The discharge conditions are the same as in Figures 1 and 2.

In Figure 6, the density profiles of two cation species,  $SF_3^+$  and  $Ar^+$ , at three selected simulating times,  $10^{-4}$ s, 0.01 s, and 1.0 s, are shown. Upon increasing the simulating time, the original coagulation of  $SF_3^+$  under the coil is totally dispersed and new coagulation is formed along the central axis, as shown in Figure 6a–c. Nevertheless, the coagulation of  $Ar^+$  is not changed with the time in Figure 6d–f. Furthermore, the collapse of cation coagulation is also caused by the expelling effect between the coagulated structures that carry positive charges, after they are treated as point-charge models as well. In addition, the dispersion of coagulation of cations (totally disappeared) is severe than the anions in Figure 5. Moreover, in the collapsing processes of both anions and cation it is found

the lighter the species is, the easier the coagulation is. Concretely, in Figures 5 and 6, the coagulation of the anion species,  $F^-$ , that are lighter than  $SF_6^-$  and  $SF_5^-$ , and the coagulation of the cation species,  $Ar^+$ , that are lighter than  $SF_3^+$ , are not dispersed.

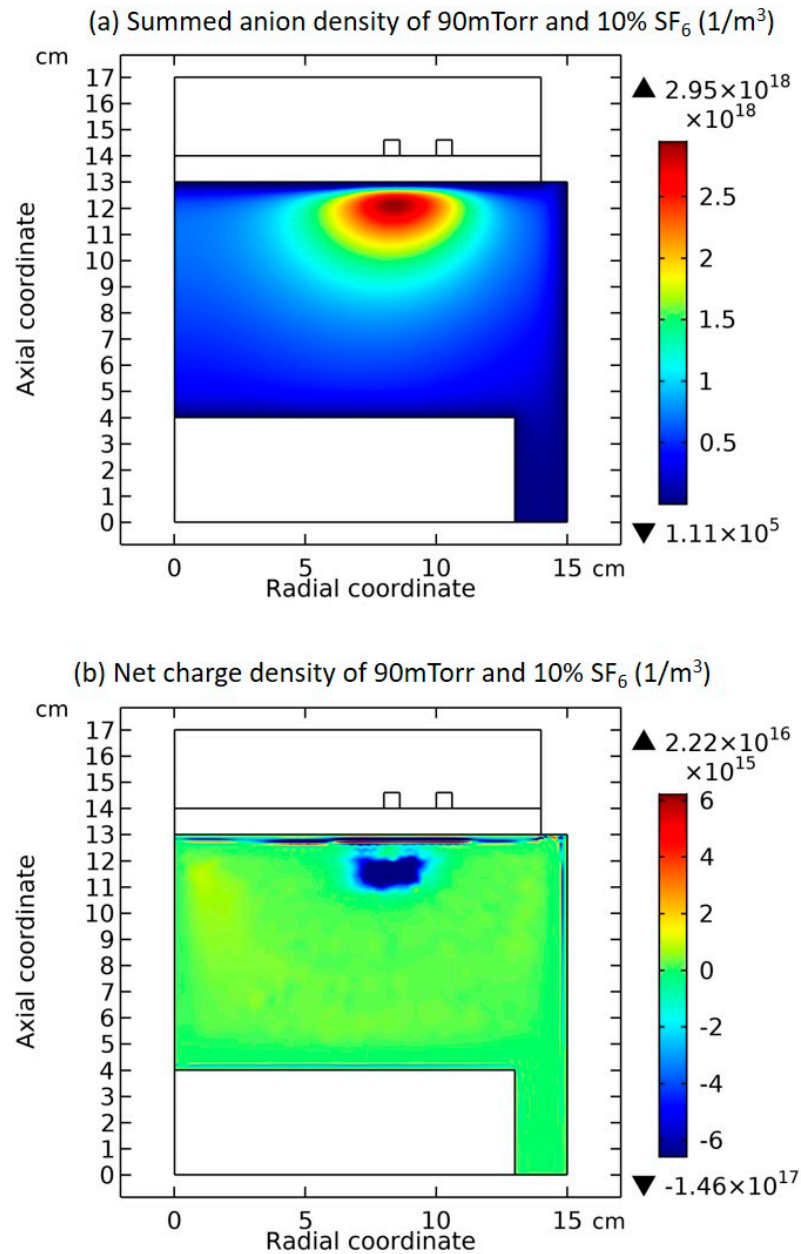


**Figure 4.** Simulated two-dimensional profiles of (a) summed anions density and (b) net charge density in Ar/ $SF_6$  plasma by means of fluid model and at the discharge conditions of 300 W, 90 mTorr, and a 10%  $SF_6$  content.

In Figure 7, more details on the collapse of the  $SF_3^+$  coagulated structure are given at four selected simulating times. In Figure 8, the charge density profiles of Ar/ $SF_6$  plasma at the above four times are given. It is seen from Figures 7 and 8 that the dispersion of  $SF_3^+$  species creates the positive charge cloud that is spatially radiative in the periphery of the original coagulated structure. The simulation shows the radiative charge cloud is not compressed into a layer (i.e., thin sheath) by means of the Debye's shield. It belongs to the anti-collective behavior of electronegative plasma that is coagulated.

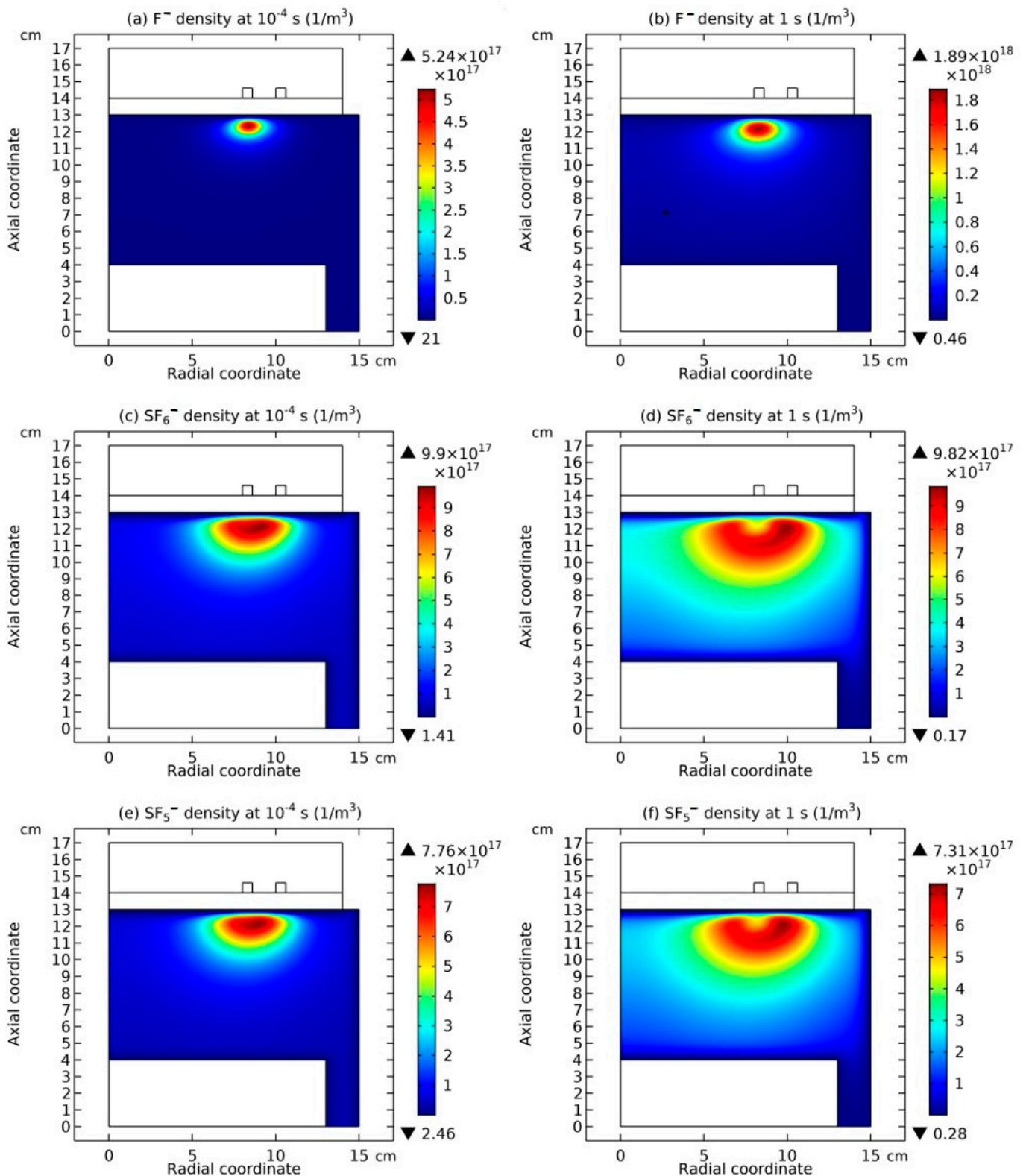


**Figure 5.** Simulated two-dimensional profiles of certain individual anions densities,  $F^-$ ,  $SF_6^-$ , and  $SF_5^-$  at two simulating times,  $10^{-4}$  s and 1.0 s. Panels (a,c,e) present the densities of  $F^-$ ,  $SF_6^-$ , and  $SF_5^-$  at an earlier time,  $10^{-4}$  s, and panels (b,d,f) present the densities of  $F^-$ ,  $SF_6^-$ , and  $SF_5^-$  at a later time, 1.0 s. The discharge conditions are the same as in Figure 4.

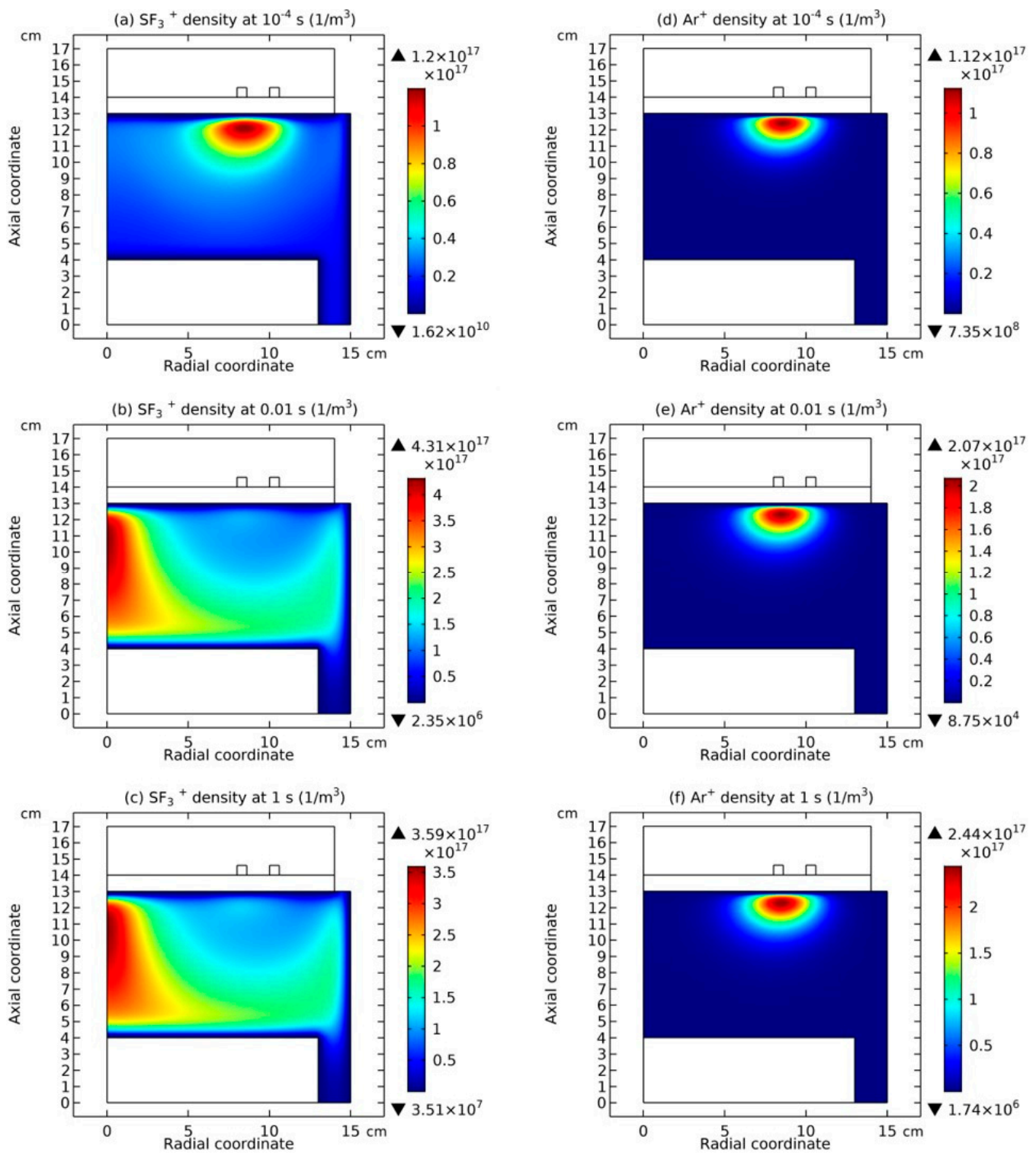


**Figure 6.** Simulated two-dimensional profiles of certain individual cations densities,  $SF_3^+$  and  $Ar^+$ , at three simulating times,  $10^{-4}$  s,  $10^{-2}$  s, and 1.0 s. Panels (a,d) present the densities of  $SF_3^+$  and  $Ar^+$  at an earlier time,  $10^{-4}$  s. Panels (b,e) present the densities of  $SF_3^+$  and  $Ar^+$  at an intermediate time,  $10^{-2}$  s. Panels (c,f) present the densities of  $SF_3^+$  and  $Ar^+$  at a later time, 1.0 s. The discharge conditions are the same as in Figure 4.

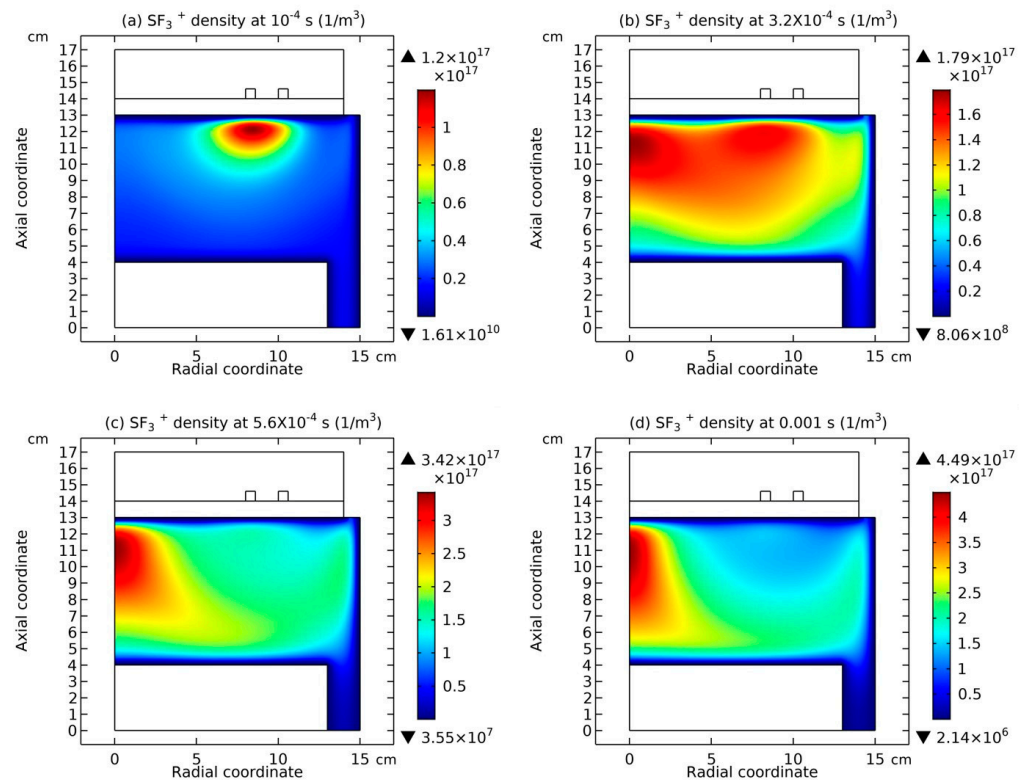


**Figure 7.** Simulated two-dimensional profiles of cation density,  $SF_3^+$ , at four simulating times: (a)  $10^{-4}$  s, (b)  $3.2 \times 10^{-4}$  s, (c)  $5.6 \times 10^{-4}$  s, and (d)  $10^{-3}$  s. The discharge conditions are the same as in Figure 4.

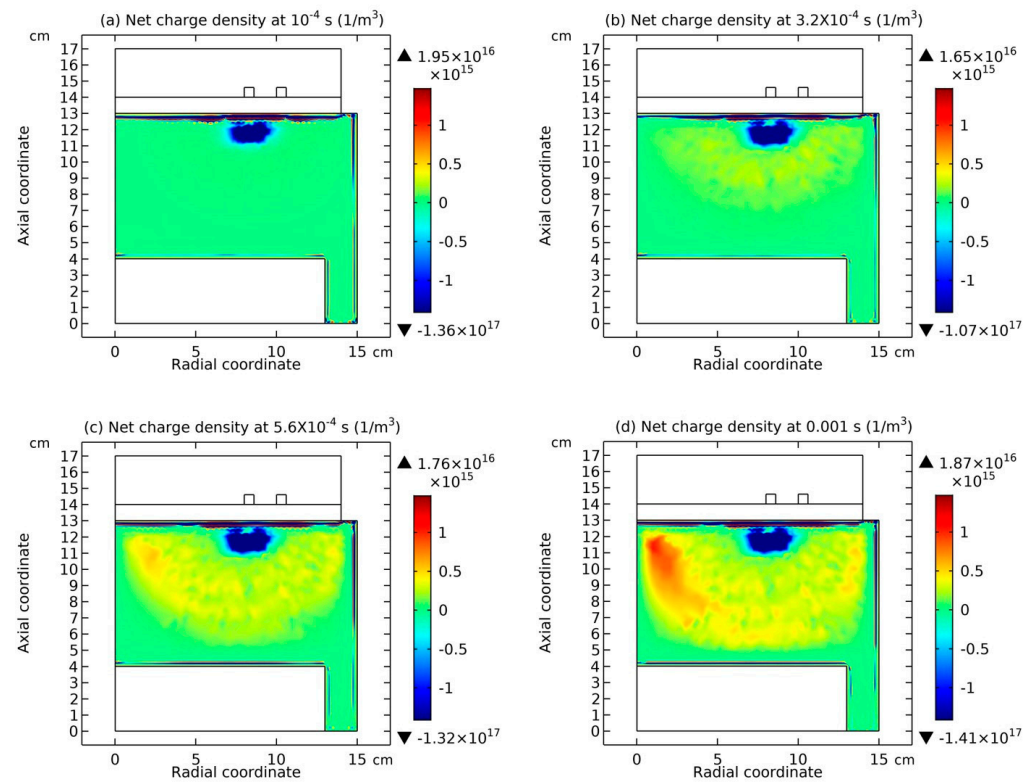


**Figure 8.** Simulated two-dimensional profiles of net charge density of Ar/ $SF_6$  plasma at four simulating times: (a)  $10^{-4}$  s, (b)  $3.2 \times 10^{-4}$  s, (c)  $5.6 \times 10^{-4}$  s, and (d)  $10^{-3}$  s. The discharge conditions are the same as in Figure 4.

### 3.4. Rebuilding of Coagulated Structure by Minor Species

In this section, it is shown that the minor cations of Ar/SF<sub>6</sub> plasma, e.g., F<sup>+</sup> cation in Figure 9, re-self-coagulate after the expelling behavior of coagulated structures when they are treated as point-charge models. The position of re-self-coagulation is selected at the discharge axis where it is easier for species assembling (geometric effect), hence forming negative source therein as shown in Figure 10. In addition, the drift of ambipolar potential is not reached for this region (refer further to Section 4.2.2(c)), hence providing the free diffusion condition. It is noted that the original F<sup>+</sup> coagulation under the coil is not influenced, where the ambipolar self-coagulation holds. One more minor cation, S<sup>+</sup>, re-self-coagulates in Figures 11 and 12. The difference is that it experiences two attempts for finishing the re-self-coagulation. The first attempt in Figure 11 failed as the forming negative source location is far away from the positive source that is near the coil. The precursor species of negative source arises from the positive source normal transport. If the communication channel of them is cut the self-coagulation halts. The finally formed negative source of S<sup>+</sup> is presented in Figure 13. One more distinction is that the S<sup>+</sup> re-self-coagulation is not that strong as the F<sup>+</sup> cation, again caused by the mass difference. Other minor cations (refer further to Section 4.3), e.g., SF<sup>+</sup> and SF<sub>2</sub><sup>+</sup>, fail to re-self-coagulate also because of their relatively large masses. The minor cations re-self-coagulation has important astronomic significance as it correlates the formation of extraterrestrial objects. In Section 4.4, it is shown that the re-self-coagulation behavior of minor species shown herein, together with the decoupled dynamics of electrons in Section 4.2.2, belongs to the spontaneous and monopolar self-coagulation.

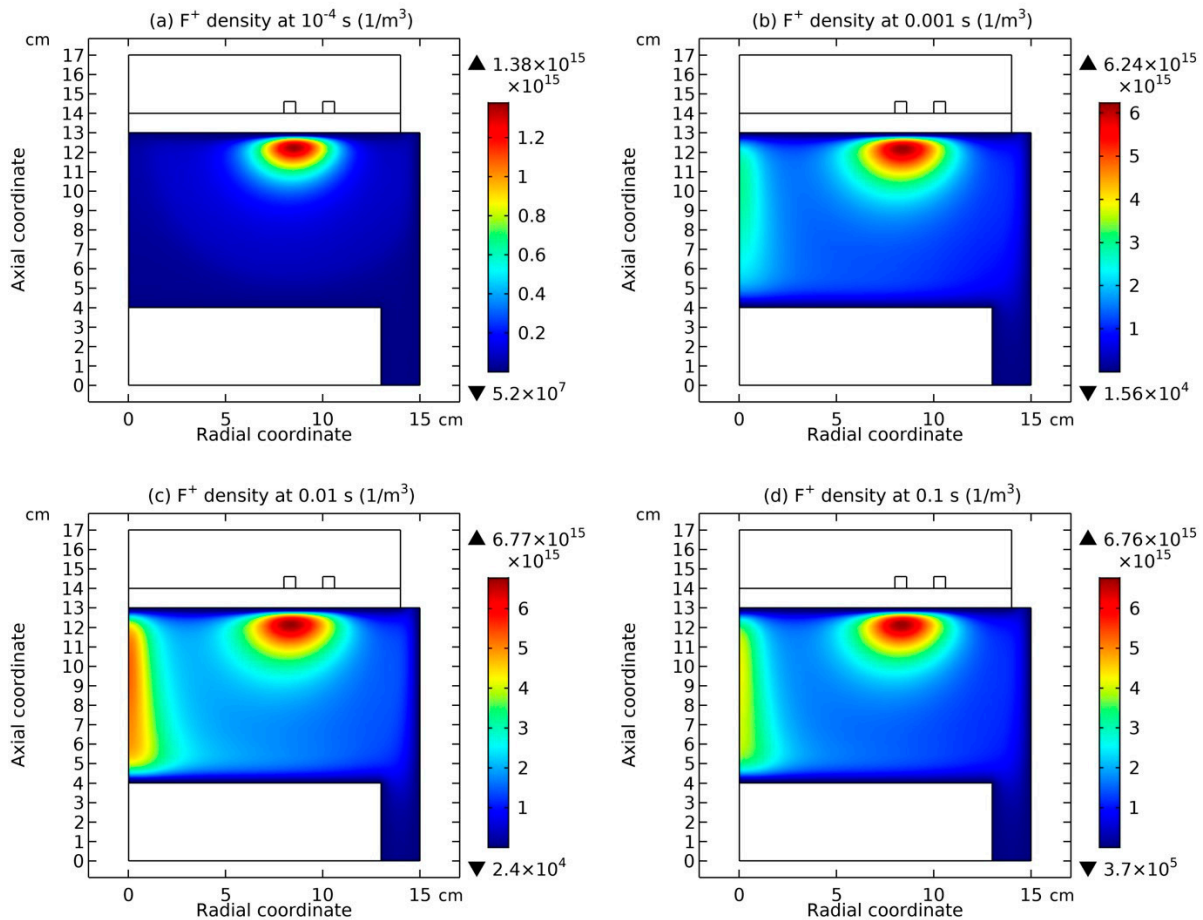


**Figure 9.** Simulated two-dimensional profiles of cation density, F<sup>+</sup>, at four simulating times, (a) 10<sup>−4</sup> s, (b) 10<sup>−3</sup> s, (c) 10<sup>−2</sup> s, and (d) 10<sup>−1</sup> s. The discharge conditions are the same as in Figure 4.

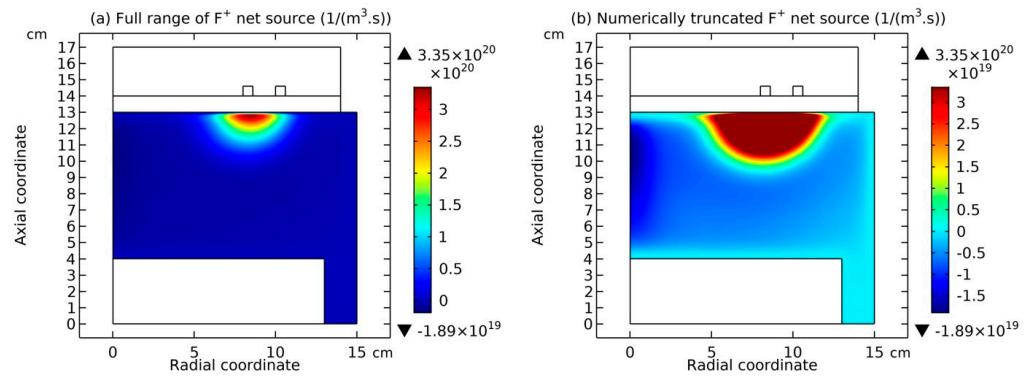


**Figure 10.** Simulated two-dimensional profile of net chemical source,  $F^+$ , in (a) full range and (b) numerically truncated range. Refer to the maxima of legends of panels (a,b). The discharge conditions are the same as in Figure 4.

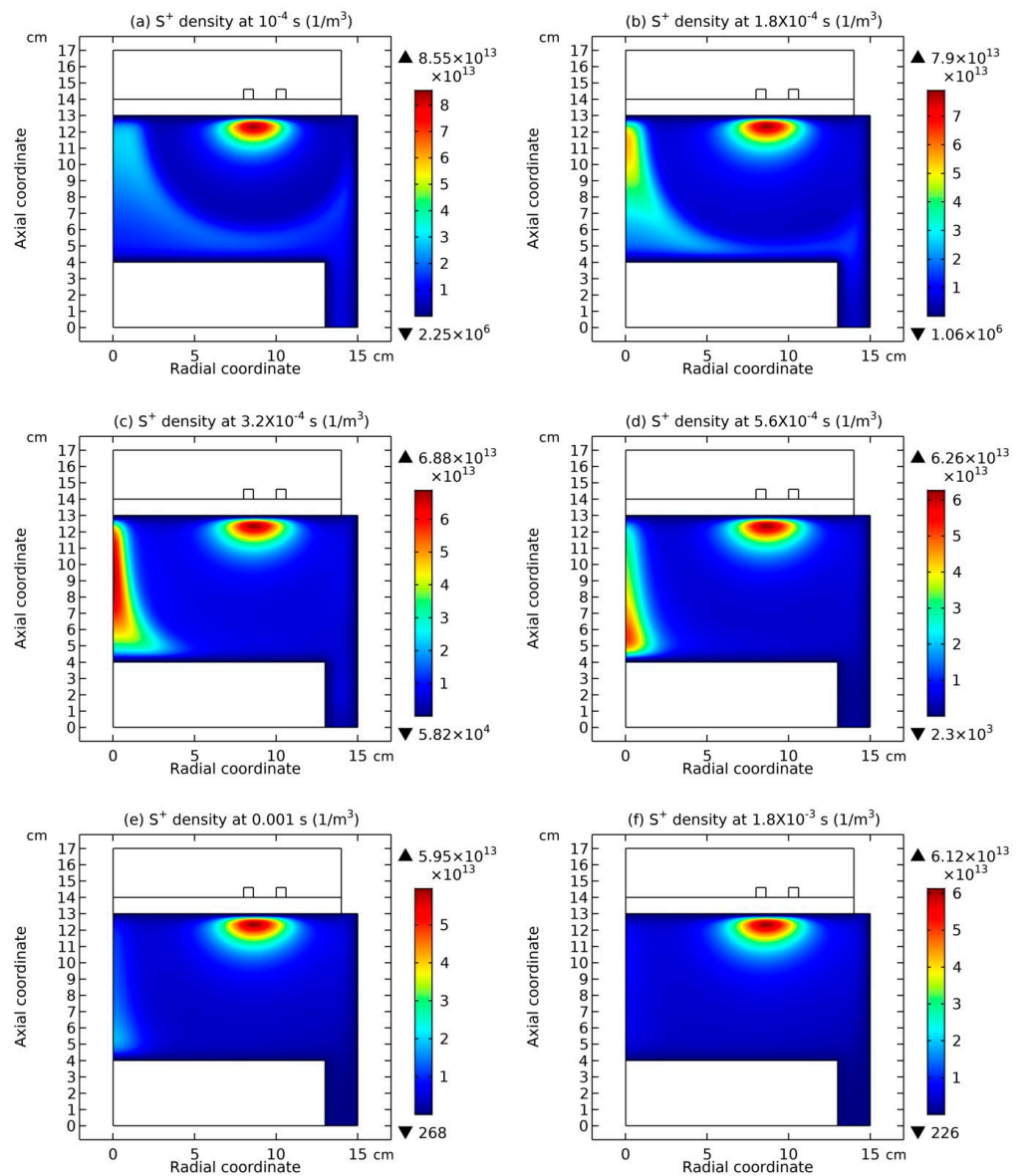


**Figure 11.** Simulated two-dimensional profiles of cation density,  $S^+$ , at six *early* simulating times, (a)  $10^{-4}$  s, (b)  $1.8 \times 10^{-4}$  s, (c)  $3.2 \times 10^{-4}$  s, (d)  $5.6 \times 10^{-4}$  s, (e)  $10^{-3}$  s, and (f)  $1.8 \times 10^{-3}$  s. The discharge conditions are the same as in Figure 4.

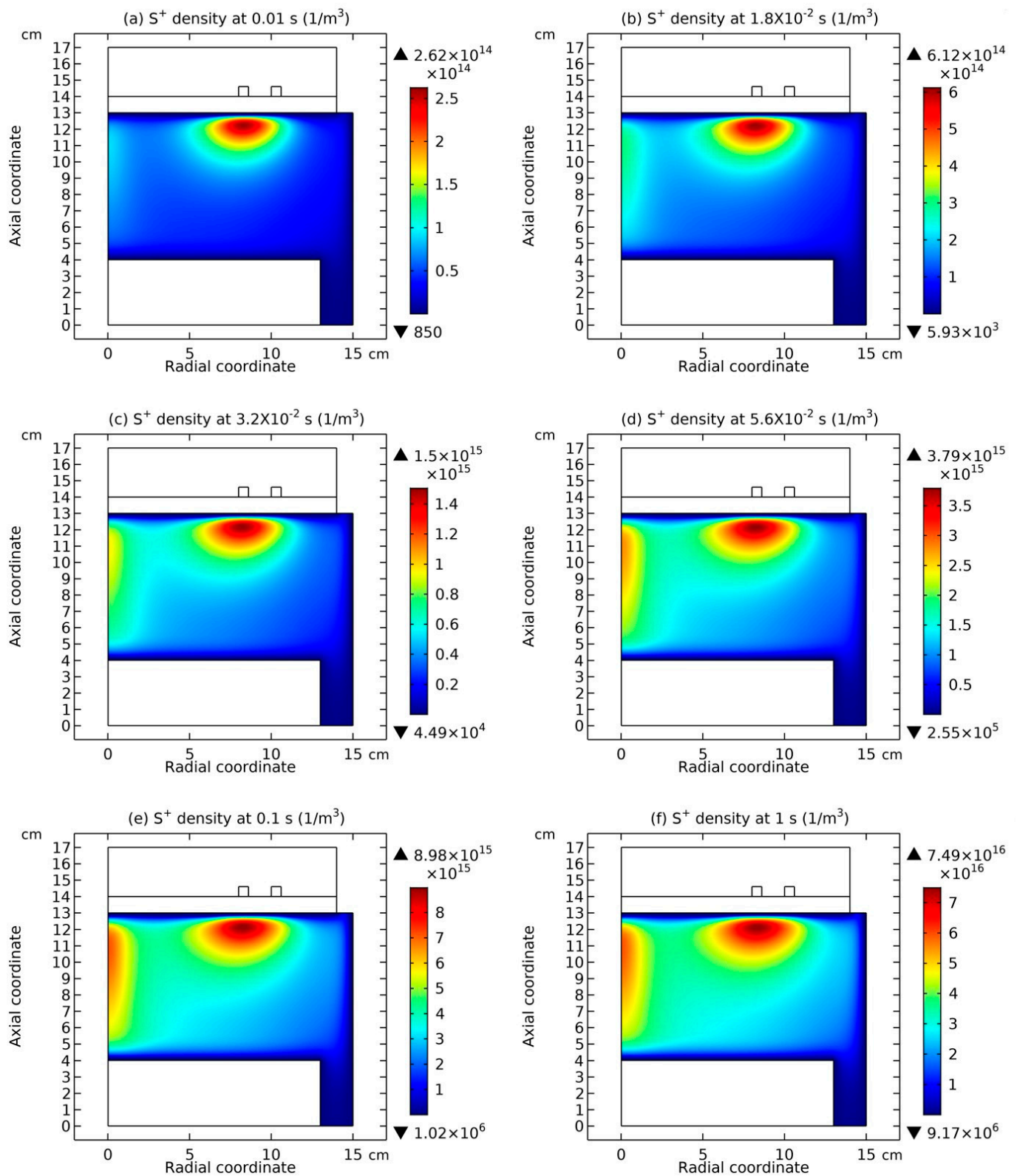


**Figure 12.** Simulated two-dimensional profiles of cation density,  $S^+$ , at six late simulating times, (a)  $10^{-2}$  s, (b)  $1.8 \times 10^{-2}$  s, (c)  $3.2 \times 10^{-2}$  s, (d)  $5.6 \times 10^{-2}$  s, (e)  $10^{-1}$  s, and (f) 1.0 s. The discharge conditions are the same as in Figure 4.

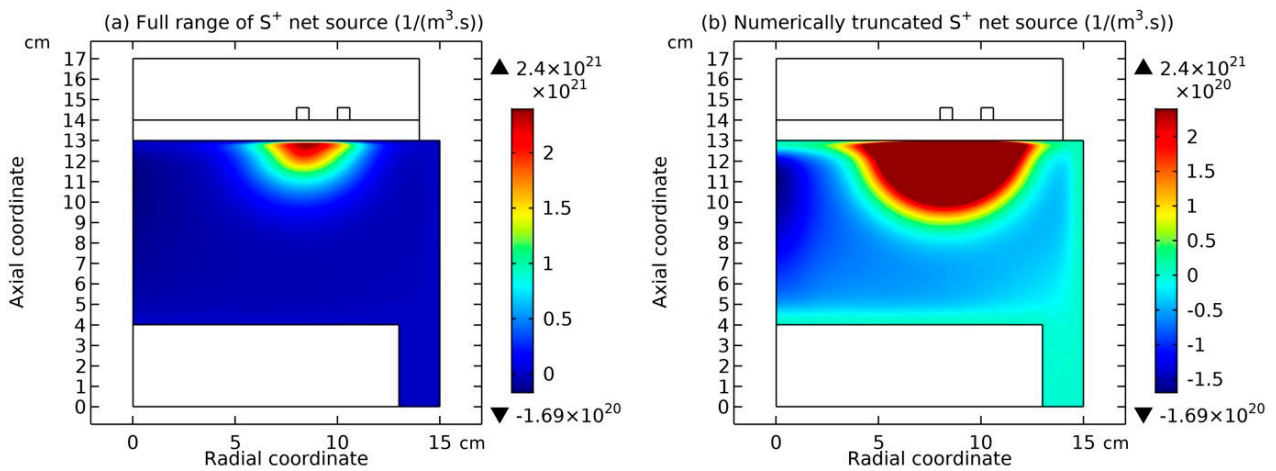


**Figure 13.** Simulated two-dimensional profile of net chemical source,  $S^+$ , in (a) full range and (b) numerically truncated range. Refer to the maxima of legends of panels (a,b). The discharge conditions are the same as in Figure 4.

#### 4. Discussion

In Section 4.1, the self-coagulation theory is built by means of the free diffusion component and negative chemical source, which explains the formations of both comet- and semi-circle shaped coagulated structures. In Section 4.2, the concepts of advective type and ambipolar type of self-coagulation are constructed sequentially, which explains the co-existence of blue sheath and electrically neutral plasma core. In Section 4.3, the expelling effect between the coagulated structures of certain Ar/SF<sub>6</sub> plasma species with the same charge type is investigated and it is found that the Coulomb’s force is maximal when the charge amounts of two point-charge models that have evolved from two selected coagulated structures in the process of scattering, are equal. This explains well the disperse and collapse of coagulated structures. In Section 4.4, the formula for the monopolar and spontaneous type of self-coagulation is given, which explains the rebuilding of coagulated structure by Ar/SF<sub>6</sub> plasma minor species at the discharge symmetrical center and the self-coagulation of electrons in the periphery of main coagulated structure beneath the coil. The coagulation of minor cation species at the discharge center is positive polarity and the coagulation of electrons in the periphery of main structure is negative polarity.

##### 4.1. Self-Coagulation Theory

The steady-state continuity equation of anions that consists of free diffusion flux and negative source term (represented by the recombination) is expressed in Equation (22).

$$-D_- \nabla^2 n_- = -n_- n_+ k_{rec} = -n_- \nu_{rec}. \quad (22)$$

Slightly reforming the Equation (22) and meanwhile introducing a parameter,  $k_-$ , a quasi-Helmholtz equation is constructed in Equation (23).

$$\begin{aligned} \nabla^2 n_- - n_- \frac{\nu_{rec}}{D_-} &= \nabla^2 n_- - n_- k_-^2 = 0, \\ \nabla^2 n_- - n_- k_-^2 &= 0. \end{aligned} \quad (23)$$

Herein,  $k_-^2 = \frac{\nu_{rec}}{D_-}$ . For simplicity, in Equation (24), all the subscripts of quantities are omitted.

$$\nabla^2 n - nk^2 = 0. \quad (24)$$

In Equation (25), this quasi-Helmholtz equation is reformed by the method of separation of variables in the cylindrical coordinate system, at the assumption of azimuthal symmetry.

$$\begin{aligned} \frac{1}{\rho} \frac{\partial}{\partial \rho} \left( \rho \frac{\partial n}{\partial \rho} \right) + \frac{\partial^2 n}{\partial z^2} - k^2 n &= 0, \\ n(\rho, z) &= R(\rho)Z(z), \\ Z'' + \nu^2 Z &= 0, \\ \frac{d^2 R}{d\rho^2} + \frac{1}{\rho} \frac{dR}{d\rho} - (k^2 + \nu^2)R &= 0. \end{aligned} \tag{25}$$

Herein,  $\nu^2$  represents the eigenvalues. By means of utilizing the homogeneous boundary conditions of the axial and ordinary differential equation,  $Z'' + \nu^2 Z = 0$ , the eigenvalues of  $\nu^2$  and the eigen functions,  $Z_m(z)$ , are acquired in Equation (26).

$$\begin{aligned} \nu_m^2 &= m^2 \pi^2 / l^2, \\ Z_m &= \sin(m\pi z / l), \\ Z &= \sum_{m=0}^{\infty} c_m Z_m = \sum_{m=0}^{\infty} c_m \sin(m\pi z / l). \end{aligned} \tag{26}$$

As noticed, the radial and ordinary differential equation,  $\frac{d^2 R}{d\rho^2} + \frac{1}{\rho} \frac{dR}{d\rho} - (k^2 + \nu_m^2)R = 0$ , is one zero-order imaginary Bessel equation, because of the property of negative source. Considering that the density value is limited at the axial center, the imaginary Bessel function, not the Hankel function, is adopted. Then, we obtain the expression of  $R(\rho)$  as follows in Equation (27).

$$R(\rho) = d_m I_0(\sqrt{k^2 + \nu_m^2} \rho) = d_m I_0(\sqrt{k^2 + m^2 \pi^2 / l^2} \rho). \tag{27}$$

Finally, we obtain the expression of  $n(\rho, z)$  in a product of  $R(\rho)$  and  $Z_m(z)$  in Equation (28).

$$\begin{aligned} n(\rho, z) &= R(\rho)Z_m(z) = \sum_{m=0}^{\infty} c_m \sin(m\pi z / l) \cdot d_m I_0(\sqrt{k^2 + \nu_m^2} \rho) \\ &= \sum_{m=0}^{\infty} a_m \sin(m\pi z / l) \cdot I_0(\sqrt{k^2 + m^2 \pi^2 / l^2} \rho). \end{aligned} \tag{28}$$

Next, some special mathematical skills, i.e., the limit idea, are used in Equation (29) and a delta distribution that is independent on the spatial coordinates is obtained, which interprets the self-coagulation idea.

$$\begin{aligned} n(\rho, z) &= R(\rho)Z_m(z) = \sum_{m=0}^{\infty} a_m \sin(m\pi z / l) \cdot I_0(\sqrt{k^2 + m^2 \pi^2 / l^2} \rho) \\ &= \lim_{m \rightarrow \infty} [a_m \sin(m\pi z / l) \cdot \infty] = \lim_{m \rightarrow \infty} \left[ a_m \sin(m\pi z / l) \cdot \lim_{z \rightarrow 0} \frac{1}{z} \right] \\ &= \lim_{z \rightarrow 0} \left[ \lim_{m \rightarrow \infty} a_m \sin(m\pi z / l) \cdot \frac{1}{z} \right] = \lim_{z \rightarrow 0} \left[ \lim_{m \rightarrow \infty} a_m \cdot \frac{\sin(m\pi z / l)}{z\pi / l} \cdot \frac{\pi}{l} \right] \\ &= \lim_{\zeta \rightarrow 0} \left[ \lim_{m \rightarrow \infty} a'_m \cdot \frac{1}{\pi} \frac{\sin(m\zeta)}{\zeta} \right] = \lim_{\zeta \rightarrow 0} \left[ a'_\infty \lim_{m \rightarrow \infty} \frac{1}{\pi} \frac{\sin(m\zeta)}{\zeta} \right] \\ &= a'_\infty \lim_{\zeta \rightarrow 0} \delta(\zeta). \end{aligned} \tag{29}$$

In the above deduction, the property of imaginary Bessel function,  $\lim_{x \rightarrow \infty} I_0(x) \rightarrow \infty$ , is utilized, which represents the condition of  $\lim_{m \rightarrow \infty} I_0(\sqrt{k^2 + m^2 \pi^2 / l^2} \rho) \rightarrow \infty$ . The condition when  $m \rightarrow \infty$  is chosen as the final solution. Other  $m$  values give rise to either vibrating

solutions ( $m > 1$ ), which are not suitable to describe the density positive property,  $n > 0$ , or solution with the profile that is relatively smooth, i.e.,  $m = 1$ , not in accord to the simulated localized profile. In addition, it is seen that only the limit result, i.e., the infinite  $\infty$  given by  $\lim_{m \rightarrow \infty} I_0(\sqrt{k^2 + m^2\pi^2/l^2}\rho)$ , is important, not the process, since when  $m \rightarrow \infty$ ,  $\lim_{m \rightarrow \infty} \sin(m\pi z/l)$ , which represents the infinite  $\infty$  coefficient of  $\lim_{m \rightarrow \infty} I_0(\sqrt{k^2 + m^2\pi^2/l^2}\rho)$ , is uncertain. So, an invented limit  $\lim_{z \rightarrow 0} \frac{1}{z}$ , although holding different evolving mathematic behavior with the imaginary Bessel, is used to replace the infinite given by the imaginary Bessel limit. In addition, the limit,  $\lim_{z \rightarrow 0}$ , is moved in front of another limit,  $\lim_{m \rightarrow \infty}$ , because at  $m \rightarrow \infty$ , the value of  $z$  in the expression of  $\sin(m\pi z/l)$  has no meaning, except at the point  $z = 0$ .

#### 4.2. Advective Ambipolar Self-Coagulation

In this section, the concept of advective and ambipolar self-coagulation is constructed, aimed at explaining the co-existence of the blue sheath and internal neutral plasma. Herein, the blue sheath is comparable to a red sheath, which can be used to define the electropositive sheath that is formed by the cations at the chamber border usually. The color of this type of sheath is red when the net positive charge profile of it is drawn in the rainbow format of two-dimensional space.

##### 4.2.1. Comet Structure for Advective Type

The advective type of self-coagulation is constructed based on the comet-shaped coagulated structure of Ar/O<sub>2</sub> plasma to explain the blue sheath. It applies to the blue sheath of semi-circle-shaped coagulated structure in the Ar/SF<sub>6</sub> plasma as well, as notified. In this subsection, the conventional Bohm's criterion of a red sheath at the chamber border is given in Section (a). Then, it is used to explain the formation of a blue sheath for anions since they are pre-pushed by the ambipolar potential before self-coagulating, as predicted by the early-stage simulation of O<sup>-</sup> dynamics in the Ar/O<sub>2</sub> plasma shown in Section (b). It is expected from the simulation that the directional velocity of anions after the pushing of the potential barrel probably exceeds the Bohm's velocity, hence forming the blue sheath in the bulk plasma.

##### (a). Bohm's criterion of sheath

In Equation (30), the energy conservation equation of ions in an assumption of neglecting elastic collisions is given. Herein,  $M$  is the mass of ions and  $\Phi(x)$  is the potential of sheath.  $u_s$  is the velocity of ions at the beginning of considered region, i.e.,  $x = 0$ , which is taken the interface of neutral plasma and sheath.

$$\frac{1}{2}Mu^2(x) = \frac{1}{2}Mu_s^2 - e\Phi(x). \tag{30}$$

Utilizing another assumption that neglects the inelastic collision in the sheath (i.e., without the ionization source), the continuity equation of ions evolves into Equation (31).

$$n_i(x)u(x) = n_{is}u_s. \tag{31}$$

Herein,  $n_i(x)$  is the ion density of arbitrary position and  $n_{is}$  is the constant density at  $x = 0$ , respectively. Correlating the Equations (30) and (31) and eliminating the arbitrary velocity of ions,  $u(x)$ , an expression is achieved for the ion density in Equation (32).

$$n_i(x) = n_{is} \left( 1 - \frac{2e\Phi}{Mu_s^2} \right)^{-1/2}. \tag{32}$$

In Equation (33), the Boltzmann’s relation of electron density is presented. Herein,  $n_e(x)$  is the arbitrary electron density and  $n_{es}$  is the constant density at  $x = 0$ , respectively.  $T_e$  is the electrons temperature.

$$n_e(x) = n_{es}e^{\Phi(x)/T_e}. \tag{33}$$

In Equation (34), the relation between  $n_{is}$  and  $n_{es}$  is given. As seen, they are equal since the sheath is always connected to bulk plasma. In Equation (35), the Poisson’s equation is shown. And in Equation (36), the ion density and electron density of the Poisson’s equation are replaced by the Equations (32) and (33), respectively. Herein, a new parameter,  $\xi_s$ , is introduced and the term  $e\xi_s$  represents the kinetic energy of ions at  $x = 0$ , as illustrated in Equation (37).

$$n_{es} = n_{is} = n_s, \tag{34}$$

$$\frac{d^2\Phi}{dx^2} = \frac{e}{\epsilon_0}(n_e - n_i), \tag{35}$$

$$\frac{d^2\Phi}{dx^2} = \frac{en_s}{\epsilon_0} \left[ \exp \frac{\Phi}{T_e} - \left( 1 - \frac{\Phi}{\xi_s} \right)^{-1/2} \right], \tag{36}$$

$$e\xi_s = \frac{1}{2}Mu_s^2. \tag{37}$$

In Equation (38) the reformed Poisson’s equation is to be integrated (herein a particular mathematical skill of integration is used), and in Equation (39) the integrated result is calculated by utilizing the conditions of integrating limits that are expressed in Equation (40). In Equation (39), the Taylor’s expansion is applied to the exponential function and square root function, and then an inequality is obtained in Equation (41) at the first-order approximations of these Taylor’s expansions, given by the fact that the term on the left side of Equation (39),  $\frac{1}{2} \left( \frac{d\Phi}{dx} \right)^2$ , should be larger than zero. This inequality is reformed in Equation (42) and the Bohm’s criterion of electropositive plasma for the red sheath of cations is obtained.

$$\int_0^\Phi \frac{d\Phi}{dx} \frac{d}{dx} \left( \frac{d\Phi}{dx} \right) dx = \frac{en_s}{\epsilon_0} \int_0^\Phi \frac{d\Phi}{dx} \left[ \exp \frac{\Phi}{T_e} - \left( 1 - \frac{\Phi}{\xi_s} \right)^{-1/2} \right] dx, \tag{38}$$

$$\frac{1}{2} \left( \frac{d\Phi}{dx} \right)^2 = \frac{en_s}{\epsilon_0} \left[ T_e \exp \frac{\Phi}{T_e} - T_e + 2\xi_s \left( 1 - \frac{\Phi}{\xi_s} \right)^{1/2} - 2\xi_s \right], \tag{39}$$

$$\Phi(0) = 0, \frac{d\Phi}{dx} \Big|_{x=0} = 0, \tag{40}$$

$$\frac{1}{2} \frac{\Phi^2}{T_e} - \frac{1}{4} \frac{\Phi^2}{\xi_s} \geq 0, \tag{41}$$

$$u_s \geq u_B = \left( \frac{eT_e}{M} \right)^{1/2}. \tag{42}$$

(b). Early-stage dynamics of simulated  $O^-$  species

In Figures 14 and 15, the temporal evolution of the  $O^-$  density profile in the two early stages of simulation, i.e., before the self-coagulation happens, is shown. It is seen that upon increasing the simulating time, the anions are kept to be pushed inward by the ambipolar potential due to the inefficient creation source of them (i.e., low electronegativity). In the above section, the Bohm’s criterion of cations is given, and it is meant that the ambipolar potential pulls the cations outward, and at the interface of plasma and sheath, the cations velocity exceeds the Bohm’s threshold, then forming an electropositive and red sheath.

Similarly, the anions can exceed the Bohm’s velocity threshold as well at the top of potential after the inward pushing process, then forming an electronegative and blue sheath (see Figure 3 for reference). Due to the appearance of a blue sheath, the comet structure is defined as an advective type of self-coagulation since the anions have experienced the advection of ambipolar potential before coagulating chemically. As seen next, this advective self-coagulation is also ambipolar due to the requirement of electrical neutrality. Whether electropositive or electronegative plasma is considered, neutrality is a basic condition that embodies the collective interaction of plasma, i.e., shielding the non-neutral region. The ambipolar attribute of self-coagulation is validated by a neutral core of comet structure in Figure 3b.

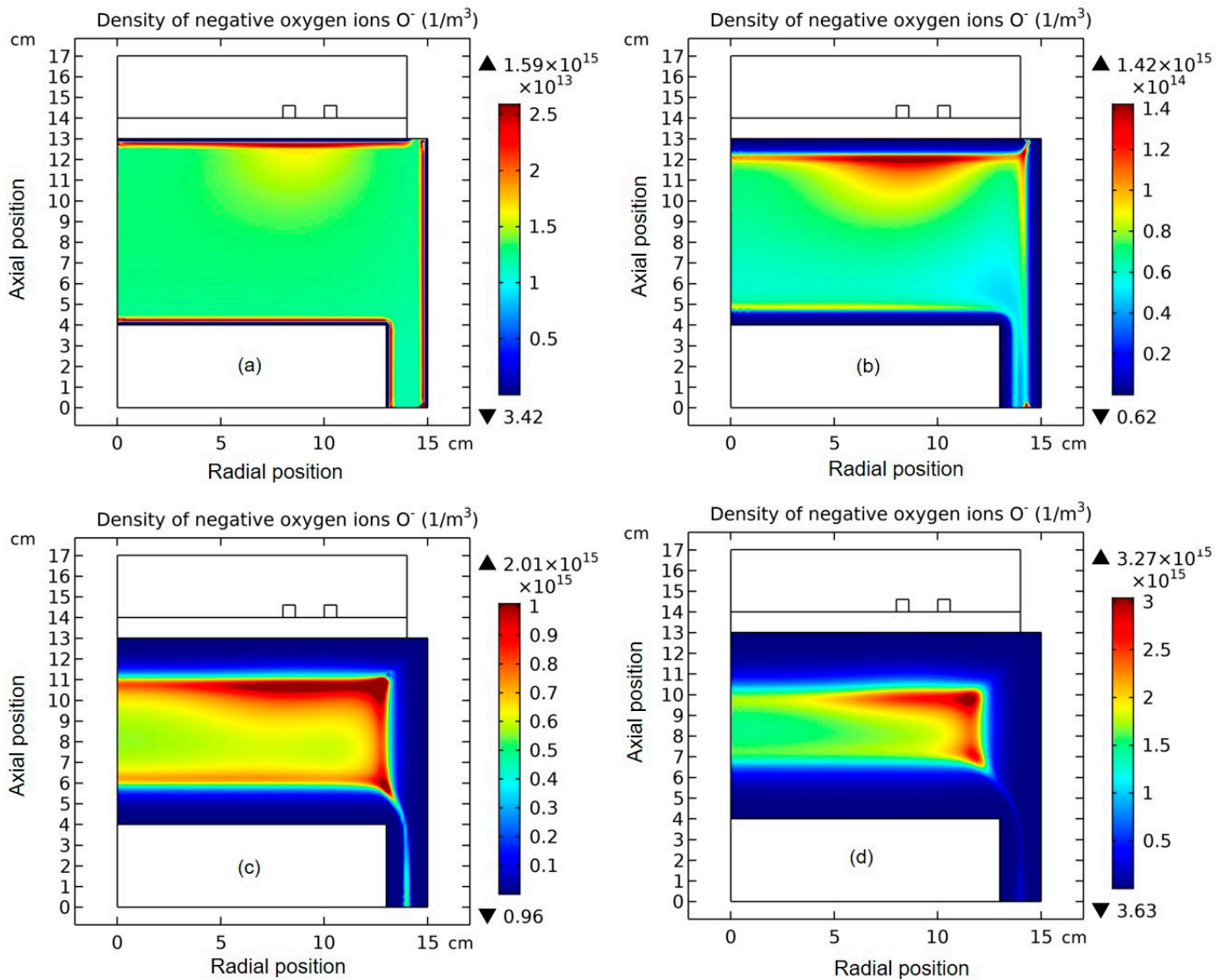


**Figure 14.** Simulated two-dimensional profiles of  $O^-$  density at the *early* stage of four simulation times, (a)  $10^{-7}$  s, (b)  $10^{-6}$  s, (c)  $5.1 \times 10^{-6}$  s, and (d)  $10^{-5}$  s, by means of fluid model. The discharge conditions are the same as Figures 1 and 2.

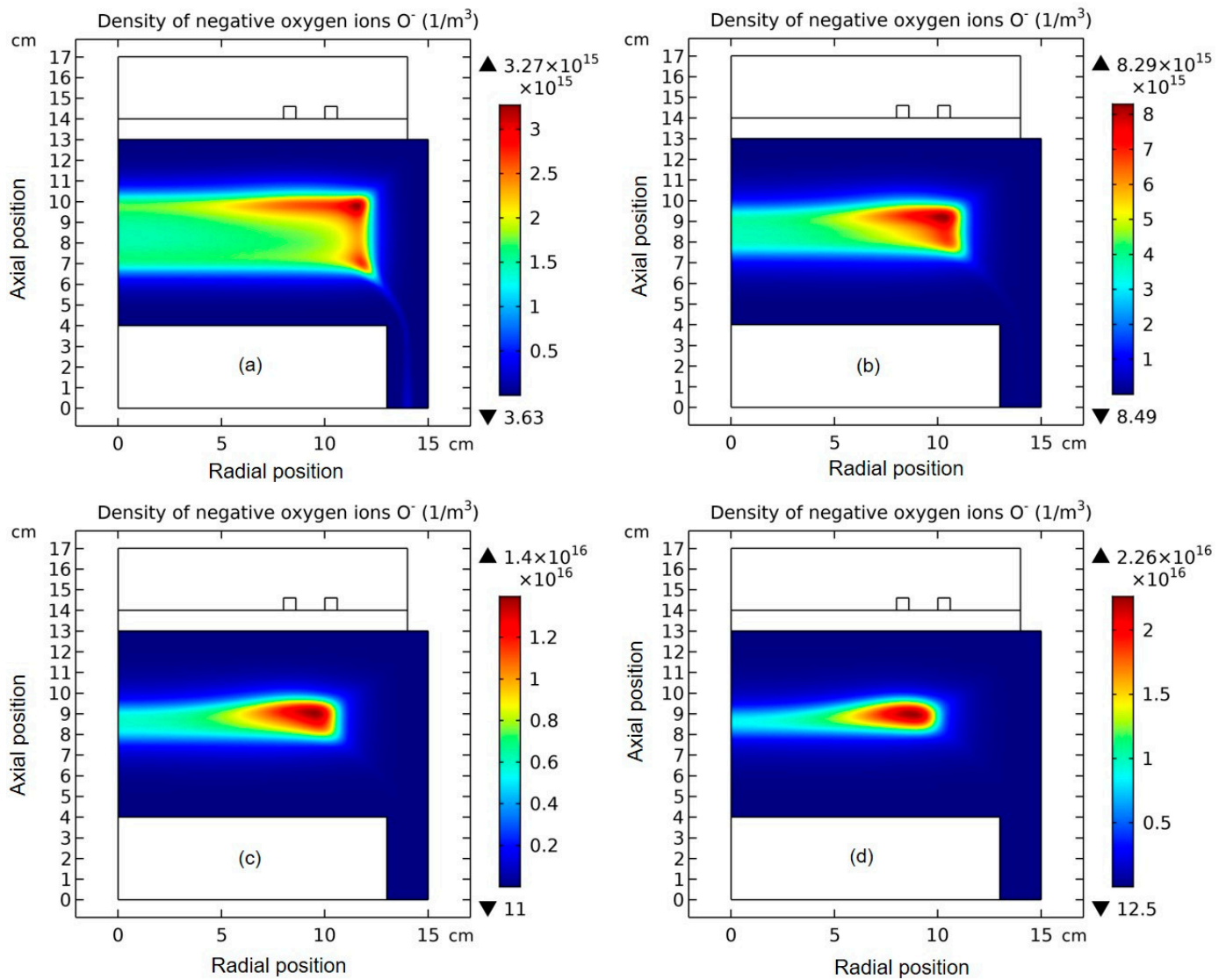


**Figure 15.** Simulated two-dimensional profiles of  $O^-$  density at the *late* stage for four simulation times, (a)  $10^{-5}$  s, (b)  $1.8 \times 10^{-5}$  s, (c)  $2.4 \times 10^{-5}$  s, and (d)  $3.2 \times 10^{-5}$  s, by means of fluid model. The discharge conditions are the same as Figures 1 and 2.

#### 4.2.2. Semi-Circle Structure for Ambipolar Type

The ambipolar type of self-coagulation is constructed based on the semi-circle-shaped coagulated structure of Ar/SF<sub>6</sub> plasma to explain the internal neutral plasma. It applies to the neutral plasma core of comet-shaped coagulated structure in the Ar/O<sub>2</sub> plasma as well, as notified. Sequentially, in Section (a), the chemical self-coagulation in the Ar/SF<sub>6</sub> plasma is compared to the physical coagulation driven by the pre-push of ambipolar potential. It is seen that the external and physical coagulation that occurs early creates the cliffy border of anion density, while the internal and chemical coagulation that occurs afterwards creates the soft border of anion density. In Section (b), the formulae of ambipolar diffusion are presented at first and then introduce the ambipolar self-coagulation concept, which is actually the collective interaction of ion-pair plasma (i.e., electrically attracting force between the anions that are being self-coagulated and the cations that are still, spatially). Different from the significant gradient that the ambipolar diffusion potential has, the ambipolar self-coagulation creates neither the potential barrel nor the potential well due to the similarity of their masses. In Section (c), due to the high electronegativity, the decouple of electron dynamics from the ambipolar self-coagulation of anion–cation pair plasma is

presented, which is characterized by the potential collapse and more expansive electron density profile than the ionic profiles.

(a). Chemical coagulation versus physical coagulation

In Figure 16, the temporal evolution of anion density that is sampled under the coil (the coordinates of sampled position can be referred to the figure) is plotted. In the time range of  $10^{-5}$  s  $\sim$   $10^{-4}$  s, the anion density increases swiftly, which indicates the self-coagulation occurrence. In Figure 17, the anions densities and their chemical source of the two times are shown, and it is validated again that the self-coagulation is accompanied by a negative source of anions in Figure 17d. Before the self-coagulation, the chemical source is positive in Figure 17c. In Figure 18, the curves of anion density close to the border under the coil are compared before and after the self-coagulation. It is seen that the curve is cliffy at  $10^{-5}$  s, which is physically formed by the pushing role of ambipolar diffusion potential and double layer [40]. The curve is then softened by the self-coagulation at  $10^{-4}$  s, implying the occurrence of chemistry process that is different to the physics process. This temporal behavior is then characterized by the mode transition from the physical coagulation to chemical coagulation. In addition, the coagulated structure found in the Ar/SF<sub>6</sub> ICP simulation is a semi-circle shape, as seen in Figure 17b.

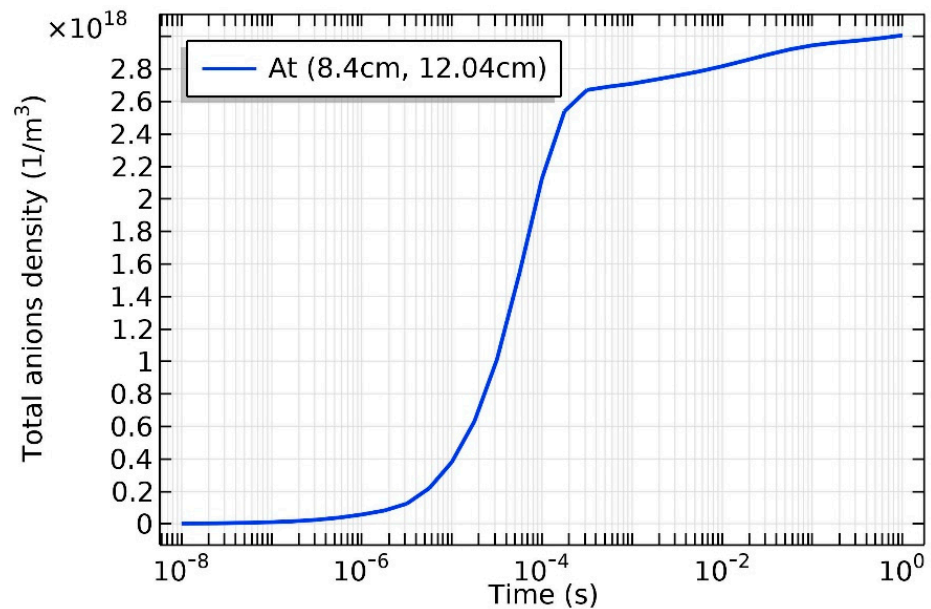


**Figure 16.** Temporal variation of simulated total anion density sampled under the coil (refer to the previous two-dimensional density profile of Figure 4a) in Ar/SF<sub>6</sub> plasma, by means of fluid model. The discharge conditions are the same as in Figure 4. The sampled position corresponds to the summed anions density peak and its coordinates are given in the figure.

(b). Ambipolar diffusion versus ambipolar self-coagulation

In Equations (43) and (44), the balances of flux and density are shown. Herein,  $\vec{\Gamma}_e$  and  $\vec{\Gamma}_i$  are the fluxes of electrons and ions, respectively. They are both equal to  $\vec{\Gamma}$ .  $n_e$  and  $n_i$  are the densities of electrons and ions, respectively. They are approximately equal to  $n$ .

$$\vec{\Gamma}_e = \vec{\Gamma}_i = \vec{\Gamma}, \tag{43}$$

$$n_e \approx n_i = n. \tag{44}$$

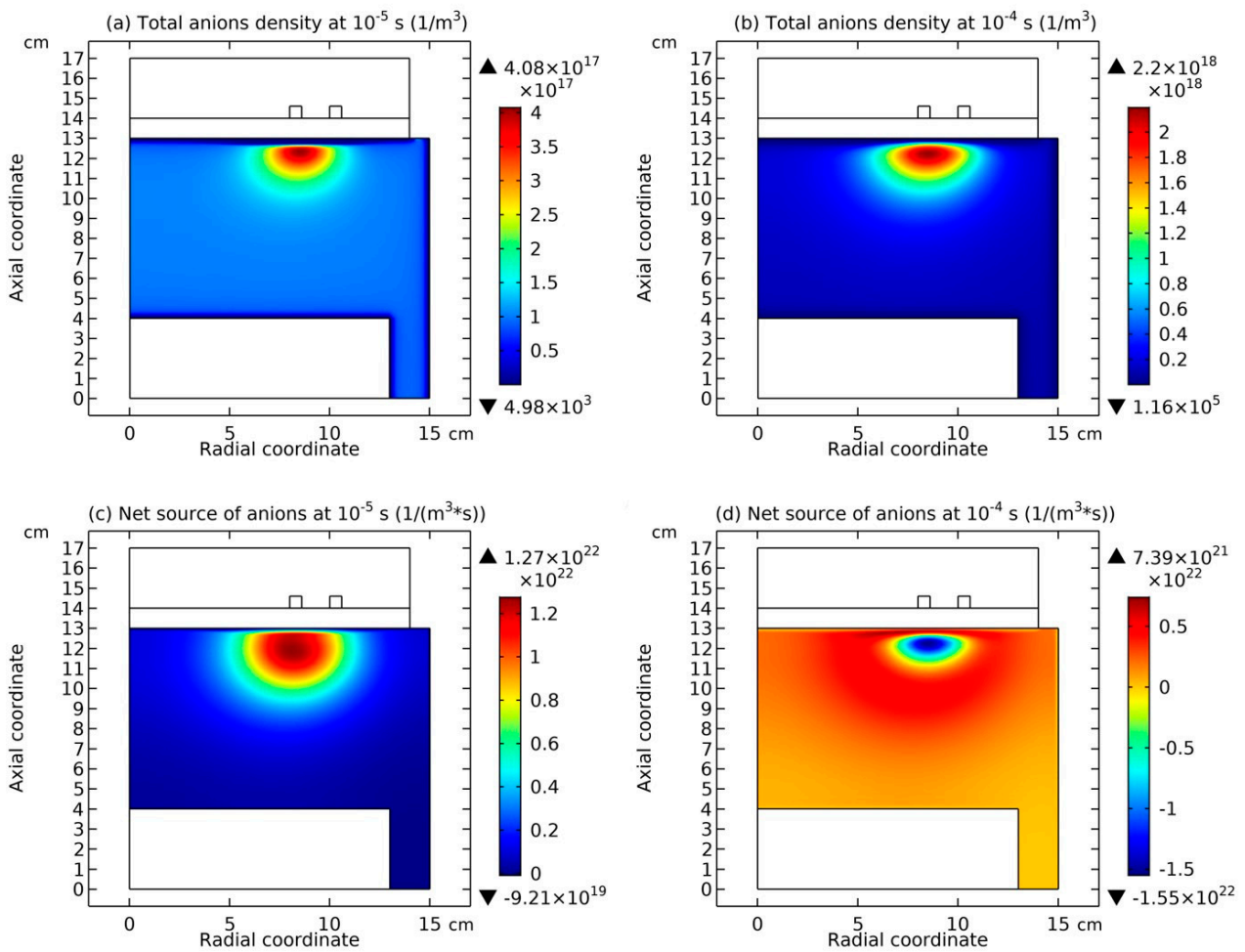


**Figure 17.** Simulated two-dimensional profiles of total anion density at two simulating times, (a)  $10^{-5}$  s and (b)  $10^{-4}$  s, and of their net chemical source at the two times, (c)  $10^{-5}$  s (before self-coagulation) and (d)  $10^{-4}$  s (after self-coagulation). The discharge conditions are the same as in Figure 4.

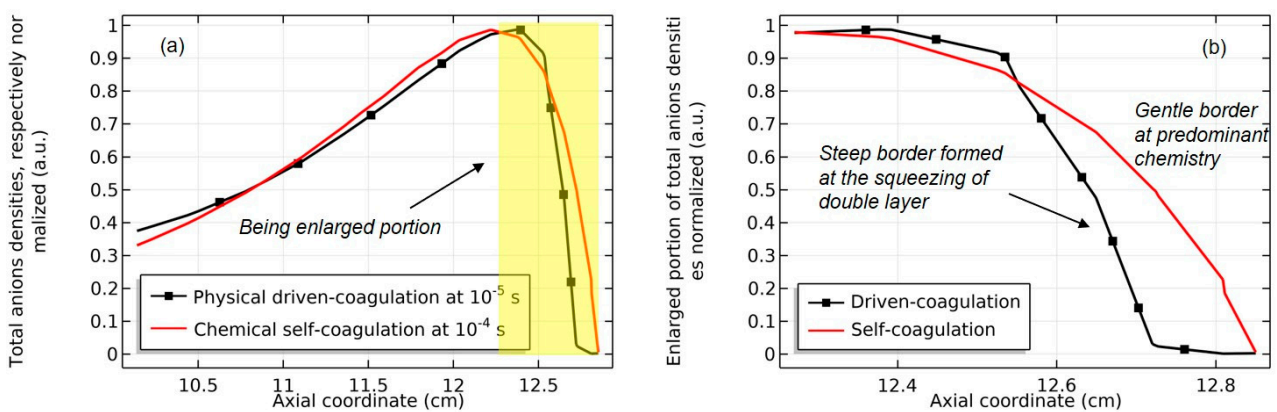


**Figure 18.** (a) Simulated and partial axial profiles of total anion density (near the coil) in Ar/SF<sub>6</sub> plasma at two simulating times,  $10^{-5}$  s (before self-coagulation) and  $10^{-4}$  s (after self-coagulation). In panel (b), the decreasing curves of total anion density border beneath the coil is enlarged to compare the curve characteristics, steep (corresponding to the physical coagulation) and gentle (corresponding to the chemical coagulation). The discharge conditions are the same as in Figure 4.

In Equation (45), the flux balance is rewritten to utilize the drift and diffusion approximation of the momentum equation. Herein,  $\mu_i$  and  $\mu_e$  are the mobilities of ions and electrons, respectively.  $D_i$  and  $D_e$  are the diffusion coefficients of ions and electrons, respectively.  $\vec{E}$  represents the electrostatic field that is caused by the ambipolar diffusion potential.

$$\mu_i n \vec{E} - D_i \nabla n = -\mu_e n \vec{E} - D_e \nabla n. \quad (45)$$

In Equation (46), the electric field is expressed as a function of the transport coefficients and density gradient. The field expression is then inserted into the flux of ions in Equation (47) and the flux is thereby reformed.

$$\vec{E} = \frac{D_i - D_e}{\mu_i + \mu_e} \frac{\nabla n}{n}, \quad (46)$$

$$\Gamma = \mu_i \frac{D_i - D_e}{\mu_i + \mu_e} \nabla n - D_i \nabla n = -\frac{\mu_i D_e + \mu_e D_i}{\mu_i + \mu_e} \nabla n. \quad (47)$$

In Equation (48), an ambipolar diffusion coefficient,  $D_a$ , is introduced based on the reformed flux. In Equation (49) the approximation between the mobilities of electrons and ions is utilized and the ambipolar coefficient is simplified. Then in Equation (50), the normally used expression of ambipolar diffusion coefficient is obtained at utilizing Einstein's relation.

$$D_a = \frac{\mu_i D_e + \mu_e D_i}{\mu_i + \mu_e}, \quad (48)$$

$$\mu_e \gg \mu_i \rightarrow D_a \approx D_i + \frac{\mu_i}{\mu_e} D_e, \quad (49)$$

$$D_a \approx D_i \left( 1 + \frac{T_e}{T_i} \right). \quad (50)$$

It is seen that the ambipolar diffusion potential is created self-consistently in the electropositive plasma because of the huge difference between the masses of electrons and ions. Without this potential barrel, all electrons escape to the chamber wall, and the gaseous discharge is extinguished. That's why the ambipolar diffusion potential established is usually high, around ten volts, as seen in the Ar/O<sub>2</sub> plasma of Figure 1d and in the early stage of simulated Ar/SF<sub>6</sub> plasma of Figure 19a (see next). The ambipolar self-coagulation discovered in electronegative plasma has the same meaning as the ambipolar diffusion, i.e., to sustain the plasma's neutrality. In particular, the ambipolar diffusion potential is used to sustain the neutrality of electrons and ions plasma, and the ambipolar self-coagulation is used to sustain the neutrality of anions and cations plasma. Since there is no obvious difference between the masses of anions and cations, the ambipolar self-coagulation potential (if existed) is not needed for sustaining the neutrality, as the simulation has predicted. It is then expected from the simulation that the cations instantaneously follow the self-coagulation of anions through the electrically appealing role between them.

### (c). Decoupled dynamics of electrons

In the highly electronegative Ar/SF<sub>6</sub> plasma, due to the existence of ambipolar self-coagulation, the dynamics of the electrons are more independent than the ions. As seen in Figure 19, after the ambipolar self-coagulation happens, the gradient of ambipolar diffusion potential that was originally established by the coupled electrons and cations system is significantly weakened. Meanwhile, the electron density profile is expanded, as shown in Figure 20. This means that the electrons dynamics are decoupled, partially from the self-coagulation behavior of ions. As seen next in Section 4.4, the electrons in the peripheral region of the semi-circle coagulated structure are sustained by spontaneous monopolar self-coagulation and not by the ambipolar diffusion potential, which has collapsed. It is noticed that in the center of the semicircle, the electrons are sustained by the ambipolar diffusion potential since the potential barrel, although collapsed, is still sustained in an order of

several volts (see Figure 19b for reference). The chemical source of electrons in the semi-circle center is positive, which is of significance for supporting the whole electronegative gaseous discharging system by providing all species needed, e.g., electrons, cations, and anions. In Figure 21, the steady-state density profiles of electrons and cations are plotted. The expansive electron density profile and the aggregative cation density profile (analogous to the anions in Figure 4a) are kept to the end in the simulation, validating the decouple of electrons and ions dynamics in the periphery of the coagulated structure. It is noted that the steady-state density profile of cations in Figure 21b is a superposition of coagulated semi-circle and dispersed ellipse (i.e., the homogeneous background). The anions profile is also a superposition of the two levels of structure, again due to the requirement of neutrality (see Figure 4a for reference). More detail about the ellipse background can be found in one of our articles related [40].

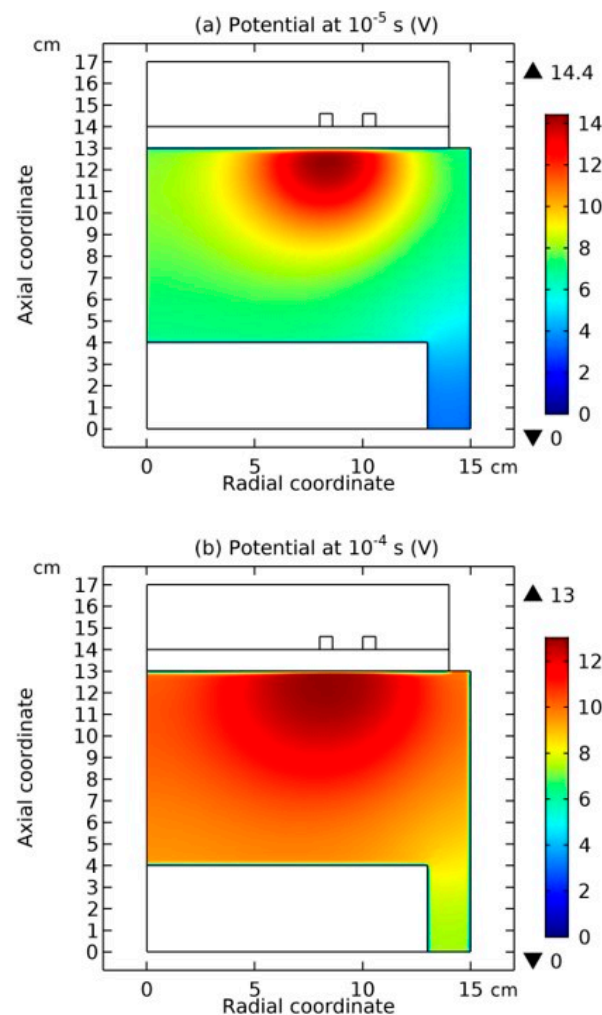


**Figure 19.** Simulated two-dimensional profiles of plasma potential at two simulating times, (a)  $10^{-5}$  s (before ambipolar self-coagulation) and (b)  $10^{-4}$  s (after ambipolar self-coagulation), in Ar/SF<sub>6</sub> plasma. The discharge conditions are the same as in Figure 4. The potential collapses along with the ambipolar self-coagulation of ions.

In addition, since the ambipolar diffusion potential was established in the early stage of the simulation, the ionic self-coagulation of Ar/SF<sub>6</sub> plasma is advective due to the early pushing role of potential by noticing the blue sheath appearing in the periphery of the semicircle in Figure 4b.

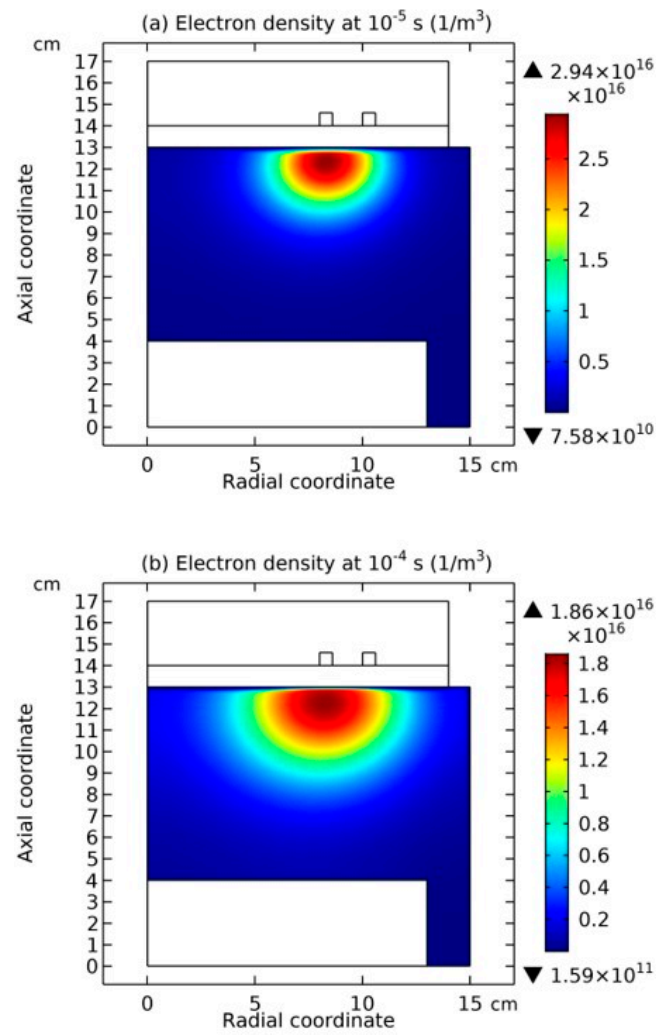


**Figure 20.** Simulated two-dimensional profiles of electron density at two simulating times, (a)  $10^{-5}$  s (before self-coagulation) and (b)  $10^{-4}$  s (after self-coagulation), in Ar/SF<sub>6</sub> plasma. The discharge conditions are the same as in Figure 4. The electron density profile expands along with the ambipolar self-coagulation of ions.

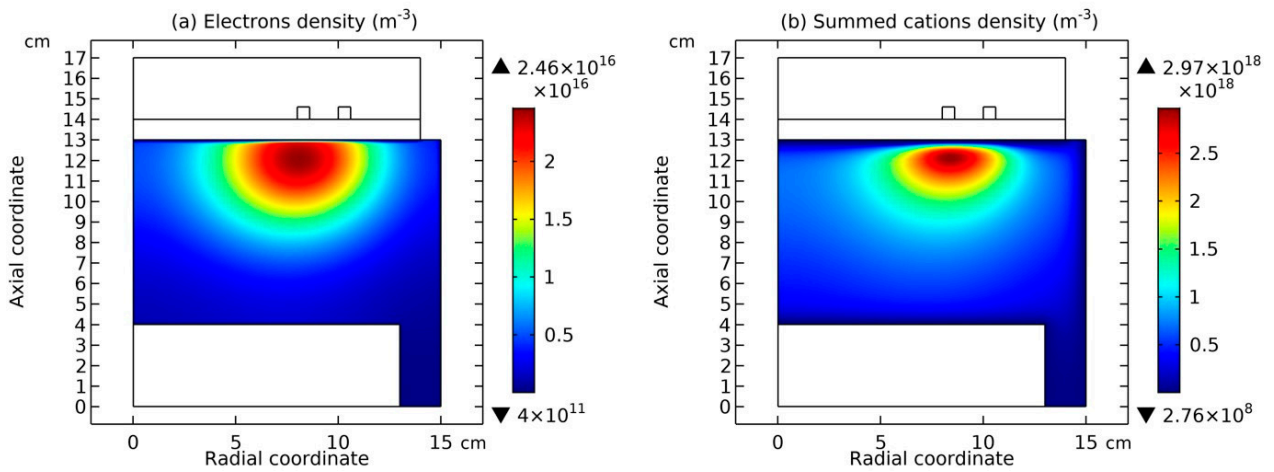


**Figure 21.** Steady-state and two-dimensional profiles of (a) electron density and (b) summed cations density, given by fluid model in Ar/SF<sub>6</sub> plasma. The discharge conditions are the same as in Figure 4.

#### 4.3. Expelling Effect between Coagulated Structures with the Same Charge Type

In Figure 22, the density peaks of different cation species in Ar/SF<sub>6</sub> plasma before the collapse of the coagulated structure are compared. In Figure 23, the density peaks of different anions species in Ar/SF<sub>6</sub> plasma before the disperse of coagulated structure are compared, and it is noticed that the densities of SF<sub>6</sub><sup>-</sup> and SF<sub>5</sub><sup>-</sup> have been summed together. It is seen from Figures 22 and 23 that the density peaks of SF<sub>3</sub><sup>+</sup> and Ar<sup>+</sup> are the most close, and the density peak of F<sup>-</sup> and the peak of summed SF<sub>6</sub><sup>-</sup> and SF<sub>5</sub><sup>-</sup> density are the most close. In Figure 24a, the Coulomb's force between the two point-charge models transformed that are positive is presented. In Figure 24b, when fixing the charge amount of two point-charge models, it is noted that Coulomb's expelling force is maximal when the charge amounts of the two models are equal. This explains the collapses of coagulated anions and cations in Figures 5 and 6 since their density peaks are the closest to their opponents shown in Figures 22 and 23. It is easily seen from Figure 24 that if the two point-charge models carry negative charge, the maximum of force still appears when the total charge amount is averaged.

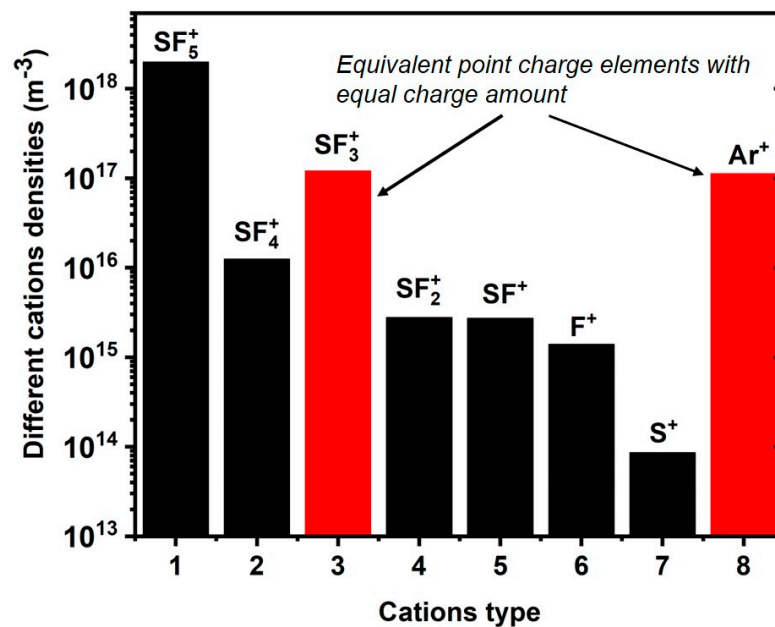


**Figure 22.** Simulated density peaks of all considered *cation species* in Ar/SF<sub>6</sub> plasma, by means of fluid model at a simulating time before the collapse happens. The discharge conditions are the same as in Figure 4. The self-coagulated density peaks of SF<sub>3</sub><sup>+</sup> and Ar<sup>+</sup> are the closest to each other, hence treated as the point-charge models (*positive type*) with equal charge amount.

In addition, in Section 3.3, the dispersion of cation coagulation in Figure 6 is more severe than the anions in Figure 5. It is caused by the fact that the coagulation of anions is a chemical process, while the coagulation of cations is a more physical process that is sustained by the ambipolar self-coagulation (see Section 4.2.2(b)). As analyzed, the ambipolar process that coagulates the cations originates from the chemical self-coagulation of anions and is ultimately sustained by means of the electrically appealing interaction between the anions and cations to keep the neutrality. Herein, the chemical factor is stronger than the physical factor.

Moreover, the light species are more coagulated, as shown in Figures 5 and 6. This is caused by the inertial effect of density quantity. In the analytical theory of Section 4.1, it is seen that the self-coagulation is caused by the negative chemical source, i.e., recombination. The dimensional analysis of Section 3.1 reveals that the chemical source can be transformed into the drift of the *effective* field, and the negative source plays the electrical role then. In the continuity equation of species, the inertial term can be multiplied by the species mass.

The electrical interaction is independent of the species mass. The species with large mass are thereby difficult to coagulate since the accelerating velocity is determined by a fixed drifting force, but for an object with a large mass this is small.

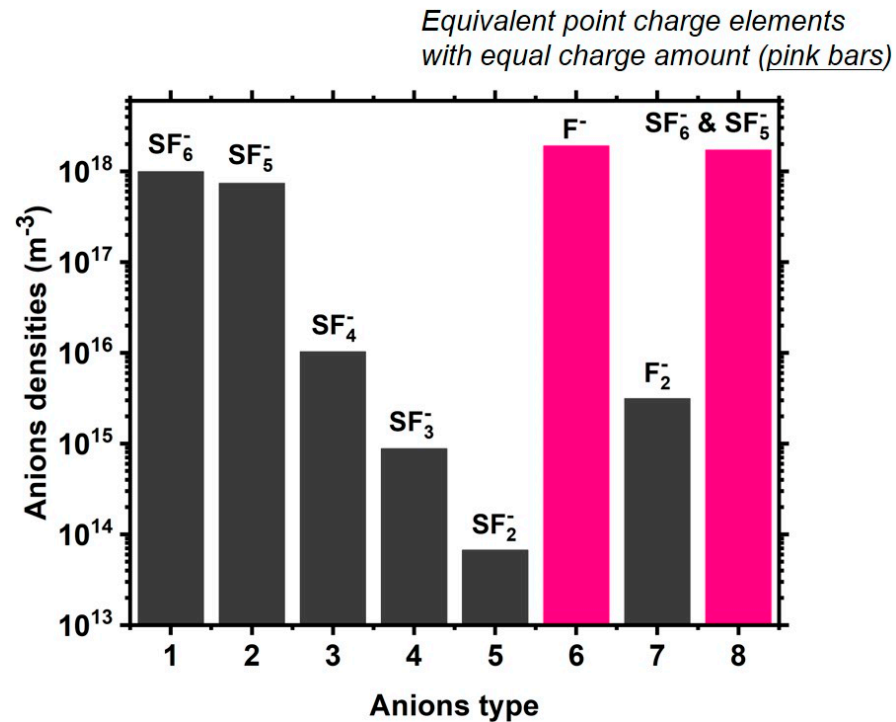
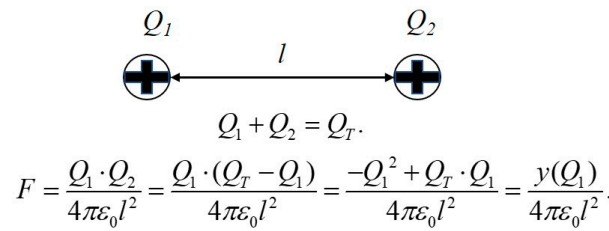


**Figure 23.** Simulated density peaks of all considered *anion species* in Ar/SF<sub>6</sub> plasma, by means of fluid model at a simulating time before the collapse happens. The discharge conditions are the same as Figure 4. The self-coagulated density peak of F<sup>-</sup> and the sum of peaks SF<sub>6</sub><sup>-</sup> and SF<sub>5</sub><sup>-</sup> are the closest to each other, hence treated as the point-charge models (*negative type*) with equal charge amount.

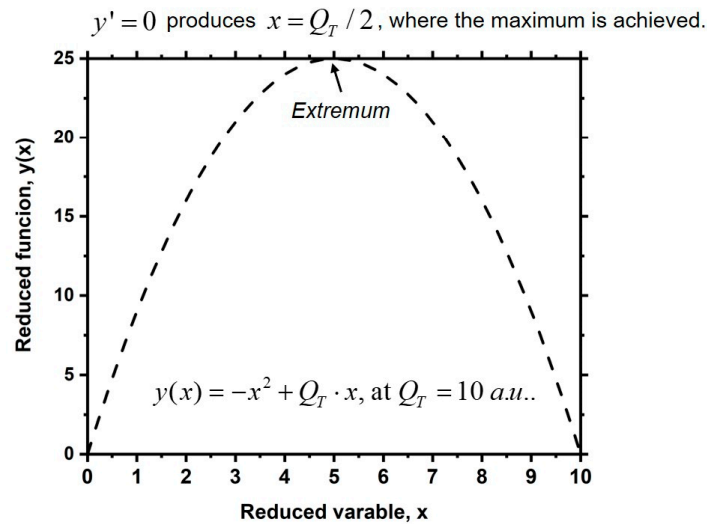
#### 4.4. Spontaneous Monopolar Self-Coagulation

In Figure 25, the simulated axial profiles of the net chemical source of electrons in Ar/SF<sub>6</sub> plasma at different simulating times are shown. It is seen that in the periphery of coagulated structure, the chemical source is negative, and it becomes more negative with time. In Section 4.2.2, it is shown that the potential collapses at increasing the time due to the decouple of electrons from ions. The collapsed potential therefore provides the free diffusion component. Together with the negative source discovered here, the self-coagulation of electrons is formed in the periphery of the coagulated structure. It is noted that the electrons self-coagulation herein, together with the re-self-coagulations of minor species in Section 3.4, is a spontaneous (i.e., non-advective) type since it has not experienced the pushing role of an ambipolar potential. In addition, the self-coagulations of electrons and minor species are also monopolar due to the decoupling feature. The formula of spontaneous and monopolar self-coagulation is described in Equation (51) and it generates the delta function at steady-state, as illustrated by the self-coagulation theory in Section 4.1. Herein,  $n$  is the species density that is to be coagulated, and  $D$  and  $\nu_{rec}$  are the free diffusion coefficients of this species and its recombination frequency, respectively. It is seen that this type of self-coagulation does not create a novel plasma-collective interaction scheme anymore due to its decoupling feature.

$$\frac{\partial n}{\partial t} - D\nabla^2 n = -n\nu_{rec}. \quad (51)$$



(a) Equivalent positive point charge models and the electric field force between them.



(b) Force versus the charge of first point charge model illustrated by a reduced function, and the extreme case, assuming specific total charge amount.

**Figure 24.** (a) Formula of expelling and the Coulomb’s force between two positive point-charge models. Herein,  $Q_1$  and  $Q_2$  are the charge amounts of two point-charges and  $Q_T$  is the total charge amount of them.  $\epsilon_0$  and  $l$  are the vacuum permittivity and the distance between them. (b) A function,  $f(x)$ , is deduced from panel (a) and its curve at the assumed constant,  $Q_T = 10$  (a.u.), is plotted. As seen, the extremum is found when the total charge amount is averaged between the two point-charges.

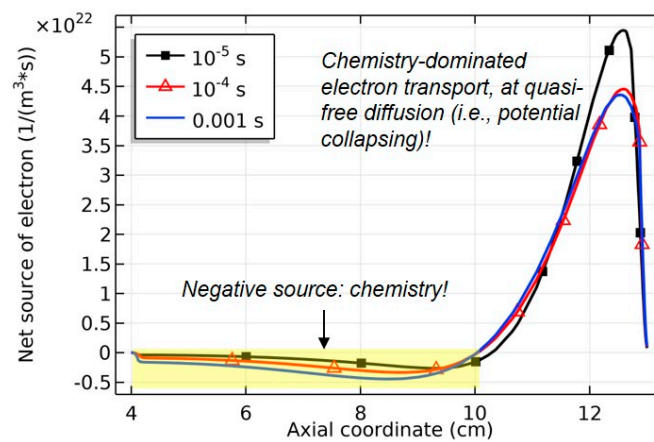


**Figure 25.** Simulated axial profiles of net chemical source of electrons at three simulating times,  $10^{-5}$  s,  $10^{-4}$  s, and  $10^{-3}$  s, given by fluid model in Ar/SF<sub>6</sub> plasma. The discharge conditions are the same as in Figure 4. At later times,  $10^{-4}$  s, and  $10^{-3}$  s, the negative chemical source and quasi-free diffusion (refer to the potential collapse in Figure 19) consist of its own monopolar self-coagulation in the yellow-high lightened periphery of semi-circle coagulated structure.

## 5. Conclusions and Further Remarks

In this article, the self-coagulation theory is formally suggested for the first time and applied to explain the coagulated structures of anions that are discovered in the fluid simulations of Ar/O<sub>2</sub> and Ar/SF<sub>6</sub> ICPs. The structure is comet-shaped in Ar/O<sub>2</sub> plasma and semi-circle-shaped in Ar/SF<sub>6</sub> plasma. To keep the neutrality, the cations have to follow the anions, therefore forming the ambipolar self-coagulation process, which is similar to the ambipolar diffusion. The ambipolar self-coagulation does not create the potential gradient since the masses of attending species, anions and cations, are almost the same. This is different from the ambipolar diffusion potential of electropositive plasma that is caused by the significant mass difference of electrons and ions. Accompanied by the self-coagulation behavior of electronegative plasma, many novel phenomena occur, such as the collapse of the coagulated structure and the blue sheath. The advective self-coagulation concept is proposed to explain the origin of the blue sheath, and based on the advective type, the anion Bohm's criterion is defined. Ar/SF<sub>6</sub> discharge generates many types of anions and cations. At the ambipolar self-coagulation, each charged heavy species has its own coagulated structure, a semi-circle. Since they are coagulated, they can be treated as point-charge models. The expelling effect of Coulomb's force existing between the individual cation or anion coagulated structures leads to the collapse or at least the dispersal of relatively weak coagulated structures. The inertial effect of density quantity explains the characteristic of self-coagulation (the lighter the species, the easier it self-coagulates), and the anti-collective property of coagulated structure is observed in the collapse of coagulated structure that creates spatially radiative charge cloud. This is different from the collective interactions of electropositive or electronegative plasmas that shield the non-neutral region into the Debye's length (see Ref. [41], pp. 7–10). There is a competition between the electron–ion system and anion–cation system. At low electronegativity, such as in the Ar/O<sub>2</sub> plasma, the electron–ion system is more coupled, and hence the conventional ambipolar diffusion potential is formed (refer to Figure 1d). Nevertheless, at high electronegativity, such as in the Ar/SF<sub>6</sub> plasma, the anion–cation system is a tight couple, and the ambipolar self-coagulation of them is more predominant. Hence, the potential collapses (refer to Figure 19), and the electron dynamics are more independent. In addition, the strong physical coagulation by means of potential barrel pushing that occurs in the early discharge stage and the static gentle chemical coagulation that occurs in the late discharge stage are compared, and they give different types of density border under the coil, cliffy and smooth, in Figure 18. The coexistence of coagulated structure and dispersed discharge background waits for the validation of related experiments that utilize either the laser detachment technique of anion that is assisted by probe diagnostics [42] or spectroscopy measurement directly [43]. The monopolar self-coagulations of minor cations and electrons have significant astrophysical meaning since they can be used to simulate the formation of extraterrestrial objects. In addition, they do not create new collective interaction mechanisms of plasma, different from the ambipolar self-coagulation.

**Author Contributions:** Conceptualization, S.Z.; methodology, S.Z.; software, Y.T.; validation, Y.T.; formal analysis, S.Z.; investigation, S.Z.; resources, Y.T.; data curation, Y.T.; writing—original draft preparation, S.Z.; writing—review and editing, Y.T.; visualization, Y.T.; supervision, Y.T. All authors have read and agreed to the published version of the manuscript.

**Funding:** This research received no external funding.

**Institutional Review Board Statement:** Not applicable.

**Informed Consent Statement:** Not applicable.

**Data Availability Statement:** The raw data supporting the conclusions of this article will be made available by the authors on request.

**Acknowledgments:** The authors are thankful to the students, An-Qi Tang and Yan-Jie Wang, who have graduated from the Dalian University of Technology, for their early contributions on constructing the Ar/SF<sub>6</sub> and Ar/O<sub>2</sub> ICP fluid models and presenting the preliminary simulation data.

**Conflicts of Interest:** The authors declare no conflicts of interest.

## References

1. Liberman, M.A.; Lichtenberg, A.J. *Principles of Plasma Discharges and Materials Processing*, 2nd ed.; Wiley-Interscience: New York, NY, USA, 2005; pp. 1–6.
2. Chabert, P.; Braithwaite, N. *Physics of Radio-Frequency Plasmas*; Cambridge University Press: New York, NY, USA, 2011; pp. 1–9.
3. Wang, S.; Xu, X.; Wang, Y.N. Numerical investigation of ion energy distribution and ion angle distribution in a dual-frequency capacitively coupled plasma with a hybrid model. *Phys. Plasmas* **2007**, *14*, 113501. [[CrossRef](#)]
4. Zhao, S.X.; Xu, X.; Li, X.C.; Wang, Y.N. Fluid simulation of the E-H model transition in inductively coupled plasma. *J. Appl. Phys.* **2009**, *105*, 083306. [[CrossRef](#)]
5. Bukowski, J.D.; Graves, D.B.; Vitello, P. Two-dimensional fluid model of an inductively coupled plasma with comparison to experimental spatial profiles. *J. Appl. Phys.* **1996**, *80*, 2614–2623. [[CrossRef](#)]
6. Lichtenberg, A.J.; Vahedi, V.; Lieberman, M.A. Modeling electronegative plasma discharges. *J. Appl. Phys.* **1994**, *75*, 2339–2347. [[CrossRef](#)]
7. Lichtenberg, A.J.; Kouznetsov, I.G.; Lee, Y.T.; Lieberman, M.A.; Kaganovich, I.D.; Tsengin, L.D. Modelling plasma discharges at high electronegativity. *Plasma Sources Sci. Technol.* **1997**, *6*, 437–449. [[CrossRef](#)]
8. Kouznetsov, I.G.; Lichtenberg, A.J.; Lieberman, M.A. Internal sheaths in electronegative discharges. *J. Appl. Phys.* **1999**, *86*, 4142–4153. [[CrossRef](#)]
9. Lampe, M.; Manheimer, W.M.; Fernsler, R.F.; Slinker, S.P.; Joyce, G. The physical and mathematical basis of stratification in electronegative plasmas. *Plasma Sources Sci. Technol.* **2004**, *13*, 15–26. [[CrossRef](#)]
10. Sheridan, T.E. Double layers in a modestly collisional electronegative discharge. *J. Phys. D Appl. Phys.* **1999**, *32*, 1761–1767. [[CrossRef](#)]
11. Chabert, P.; Sheridan, T.E. Kinetic model for a low-pressure discharge with negative ions. *J. Phys. D Appl. Phys.* **2000**, *33*, 1854–1860. [[CrossRef](#)]
12. Franklin, R.N.; Snell, J. Are the oscillations found in electronegative plasmas at low pressure an artefact? *J. Phys. D Appl. Phys.* **2000**, *33*, 1990–1995. [[CrossRef](#)]
13. Kaganovich, I. Negative ion density fronts. *Phys. Plasmas* **2001**, *8*, 2540–2548. [[CrossRef](#)]
14. Schulze, J.; Derzsi, A.; Dittmann, K.; Hemke, T.; Meichsner, J.; Donko, Z. Ionization by Drift and Ambipolar Electric Field in Electronegative Capacitive Radio Frequency Plasmas. *Phys. Rev. Lett.* **2011**, *107*, 275011. [[CrossRef](#)]
15. Liu, Y.X.; Schungel, E.; Korolov, I.; Donko, Z.; Wang, Y.N.; Schulze, J. Experimental Observation and Computational Analysis of Striations in Electronegative Capacitively Coupled Radio-Frequency Plasmas. *Phys. Rev. Lett.* **2016**, *116*, 255002. [[CrossRef](#)]
16. Zhao, S.X. Quasi-delta negative ions density of Ar/O<sub>2</sub> inductively coupled plasma at very low electronegativity. *Chin. Phys. B* **2021**, *30*, 055201. [[CrossRef](#)]
17. Zhao, S.X.; Li, J.Z. Delta distribution of electronegative plasma predicted by reformed spring oscillator dynamic equation with dispersing force. *Chin. Phys. B* **2021**, *30*, 055202. [[CrossRef](#)]
18. Carlqvist, P. On the acceleration of energetic cosmic particles by electrostatic double layers. *IEEE Trans. Plasma Sci.* **1986**, *14*, 794–799. [[CrossRef](#)]
19. Plihon, N.; Corr, C.S.; Chabert, P.; Raimbault, J.L. Periodic formation and propagation of double layers in the expanding chamber of an inductive discharge operating in Ar/SF<sub>6</sub> mixtures. *J. Appl. Phys.* **2005**, *98*, 023306. [[CrossRef](#)]
20. Hu, X.W. *Fundamental of Plasma Theory*; Peking University Press: Beijing, China, 1997; pp. 238–243, 553–561. (In Chinese)
21. Wang, W.H. Study on the Closed Fluid Mechanics Model Based on the Kinetic Theory and Self-Consistent Solution for the Transport Coefficients of Heavy Species. Ph.D. Thesis, Dalian University of Technology, Dalian, China, 7 June 2023. (In Chinese).
22. Wang, W.H.; Zhao, S.X.; Dai, Z.L. A self-consistent method for solving ion diffusion and mobility coefficients. *Phys. Plasmas* **2021**, *28*, 103503. [[CrossRef](#)]
23. Arnault, P.; Guisset, S. Chapman-Enskog derivation of multicomponent Navier-Stokes equations. *Phys. Plasmas* **2022**, *29*, 090901. [[CrossRef](#)]
24. Qiu, J.L. *Gaseous Electronics*; Huazhong Science and Technology University Press: Wuhan, China, 1999; pp. 36–39. (In Chinese)
25. Dickinson, E.J.F.; Ekstrom, H.; Fontes, E. COMSOL Multiphysics: Finite element software for electrochemical analysis. A mini-review. *Electrochem. Commun.* **2014**, *40*, 71–74. [[CrossRef](#)]
26. Cutress, I.J.; Dickinson, E.J.F.; Compton, R.G. Analysis of commercial general engineering finite element software in electrochemical simulations. *J. Electroanal. Chem.* **2010**, *638*, 76–83. [[CrossRef](#)]
27. Plasma Data Exchange Project. Available online: <https://fr.lxcat.net/instructions/> (accessed on 8 March 2020).
28. Yang, W.; Zhao, S.X.; Wen, D.Q.; Liu, W.; Liu, Y.X.; Li, X.C.; Wang, Y.N. F atom kinetics in SF<sub>6</sub>/Ar inductively coupled plasmas. *J. Vac. Sci. Technol. A* **2016**, *34*, 031305. [[CrossRef](#)]
29. Mao, M.; Wang, Y.N.; Bogaerts, A. Numerical study of the plasma chemistry in inductively coupled SF<sub>6</sub> and SF<sub>6</sub>/Ar plasmas used for deep silicon etching application. *J. Phys. D Appl. Phys.* **2011**, *44*, 435202. [[CrossRef](#)]
30. Lallement, L.; Rhallabi, A.; Cardinaud, C.; Peignon-Fernandez, M.C.; Alves, L.L. Global model and diagnostic of a low-pressure SF<sub>6</sub>/Ar inductively coupled plasma. *Plasma Sources Sci. Technol.* **2009**, *18*, 025001. [[CrossRef](#)]
31. You, Z.W.; Dai, Z.L.; Wang, Y.N. Simulations of capacitively coupled dual-frequency N<sub>2</sub>, O<sub>2</sub>, N<sub>2</sub>/O<sub>2</sub> discharge: Effects of external parameters on plasma characteristics. *Plasma Sci. Technol.* **2014**, *16*, 335–343. [[CrossRef](#)]
32. Gudmundsson, J.T.; Kouznetsov, I.G.; Patel, K.K.; Lieberman, M.A. Electronegativity of low-pressure high-density oxygen discharges. *J. Phys. D Appl. Phys.* **2001**, *34*, 1100–1109. [[CrossRef](#)]

33. Wang, Y.H.; Liu, W.; Zhang, Y.R.; Wang, Y.N. Fluid simulation of inductively coupled Ar/O<sub>2</sub> plasma: Comparisons with experiment. *Chin. Phys. B* **2015**, *24*, 095203. [[CrossRef](#)]
34. Brezmes, A.O.; Breilkopf, C. Fast and reliable simulations of argon inductively coupled plasma using COMSOL. *Vacuum* **2015**, *116*, 65–72. [[CrossRef](#)]
35. Levko, D. Decay of a low-pressure oxygen magnetized and unmagnetized plasma. *J. Appl. Phys.* **2014**, *116*, 103304. [[CrossRef](#)]
36. Hsu, C.C.; Neirode, M.A.; Coburn, J.W.; Graves, D.B. Comparison of model and experiment for Ar, Ar/O<sub>2</sub>, and Ar/O<sub>2</sub>/Cl<sub>2</sub> inductively coupled plasmas. *J. Phys. D Appl. Phys.* **2006**, *39*, 3272–3284. [[CrossRef](#)]
37. Takechi, K.; Lieberman, M.A. Effect of Ar addition to an O<sub>2</sub> plasma in an inductively coupled traveling wave driven, large area plasma source: O<sub>2</sub>/Ar mixture plasma modeling and photoresist etching. *J. App. Phys.* **2001**, *90*, 3205–3211. [[CrossRef](#)]
38. Graves, D.B.; Kiehlbauch, M.K. Inductively coupled plasmas in oxygen: Modeling and experiment. *J. Vac. Sci. Technol. A* **2003**, *21*, 660–670. [[CrossRef](#)]
39. Zhao, S.X. Non-monotonic behavior of electron temperature in argon inductively coupled plasma and its analysis via novel electron mean energy equation. *Phys. Plasmas* **2018**, *25*, 033516. [[CrossRef](#)]
40. Zhao, S.X.; Sun, Y.H. Discharge Structure Theory of Highly Electronegative Plasma. *Phys. Scr.* 2024; submitted.
41. Chen, F.F. *Introduction to Plasma Physics and Controlled Fusion*, 3rd ed.; Springer: Cham, Switzerland, 2018; pp. 7–10.
42. Du, P.C.; Gao, F.; Wang, X.K.; Liu, Y.X.; Wang, Y.N. Measurement of electronegativity during the E to H mode transition in a radio frequency inductively coupled Ar/O<sub>2</sub> plasma. *Chin. Phys. B* **2021**, *30*, 035202. [[CrossRef](#)]
43. Liu, G.H.; Wang, X.Y.; Liu, Y.X.; Sun, J.Y.; Wang, Y.N. Effects of secondary electron emission on plasma density and electron excitation dynamics in dual-frequency asymmetric capacitively coupled argon plasma. *Plasma Sources Sci. Technol.* **2018**, *27*, 064004. [[CrossRef](#)]

**Disclaimer/Publisher's Note:** The statements, opinions and data contained in all publications are solely those of the individual author(s) and contributor(s) and not of MDPI and/or the editor(s). MDPI and/or the editor(s) disclaim responsibility for any injury to people or property resulting from any ideas, methods, instructions or products referred to in the content.